

Bachelor's Thesis

Ground state phases of the t - J model on kagome strips

Grundzustands-Phasen des t - J Modells auf kagome Streifen

prepared by

Justin Kowalski

from Oldenburg

at the Institut für Theoretische Physik

Thesis period: 25th April 2024 until 3rd August 2024

Supervisor: apl. Prof. Dr. Salvatore R. Manmana

First Rreferee: apl. Prof. Dr. Salvatore R. Manmana

Second referee: Prof. Dr. Stefan Kehrein

Abstract

In this thesis the ground state phases of the t - J model on kagome strips are investigated. The ground state energy E_0 and state vector $|\psi_0\rangle$ are numerically computed with ITensor's DMRG implementation in Julia. The phases are distinguished by the results obtained for the spin gap and three different correlation functions. The singlet pairing P_{ij} , density-density N_{ij} and spin-spin S_{ij} correlation functions are computed as well as the eigenvalues of P_{ij} , which can both indicate quasi-long-range order in the system. These calculations are performed for different values of J and two fillings $n = 1/3$ and $n = 1/8$ in order to sketch a phase diagram. The results are compared with those of the t - J chain published on the literature.

Keywords: Physics, Bachelor thesis, t - J model, kagome strips, ground state phases, spin gap, superconductivity, matrix product states, order parameter, long-range order, quasi-long-range order, correlation functions

Zusammenfassung

In dieser Arbeit werden die Grundzustands-Phasen des t - J Modells auf kagome Streifen untersucht. Die Grundzustandsenergie E_0 und Zustandsvektor $|\psi_0\rangle$ werden numerisch mit ITensors DMRG Implementation in Julia bestimmt. Die Phasen werden durch die Ergebnisse der Spinlücke und drei verschiedener Korrelationsfunktionen charakterisiert. Die Singlet-Paarungs-Korrelationsfunktion P_{ij} , Dichte-Dichte-Korrelationsfunktion N_{ij} und Spin-Spin-Korrelationsfunktion S_{ij} werden berechnet sowie die Eigenwerte von P_{ij} , die beide auf quasi-langreichweitige Ordnung im System hinweisen können. Diese Berechnungen werden für verschiedene Werte von J und zwei verschiedenen Füllungen $n = 1/3$ und $n = 1/8$ durchgeführt, um ein Phasendiagramm zu skizzieren. Die Ergebnisse werden mit denen der t - J Kette verglichen, da diese veröffentlicht sind.

Stichwörter: Physik, Bachelorarbeit, t - J Modell, kagome Streifen, Grundzustands-Phasen, Spinlücke, Supraleitung, Matrixproduktzustände, Ordnungsparameter, Langreichweitige Ordnung, Quasi Langreichweitige Ordnung, Korrelationsfunktionen

Contents

| | | |
|----------|--|-----------|
| 1 | Introduction | 1 |
| 2 | Theory | 3 |
| 2.1 | Quantum Many-Body Systems | 3 |
| 2.2 | Phases and Phase Transitions | 4 |
| 2.2.1 | Order Parameters and Symmetry Breaking | 4 |
| 2.2.2 | Long-Range Order and Quasi Long-Range Order | 6 |
| 2.2.3 | BCS Theory and Superconductivity | 8 |
| 3 | Modeling | 11 |
| 3.1 | The t-J Model | 11 |
| 3.2 | Kagome Geometry | 13 |
| 3.3 | Kagome Strip | 14 |
| 3.3.1 | Mapping of the Lattice | 15 |
| 3.3.2 | Definition of Distance | 16 |
| 3.3.3 | Definition of Bonds | 16 |
| 4 | Numerical Methods | 19 |
| 4.1 | Matrix Product States | 19 |
| 4.2 | Tensor Networks | 20 |
| 4.3 | Matrix Product Operators | 21 |
| 4.4 | Density Matrix Renormalization Group | 22 |
| 4.4.1 | Truncation | 23 |
| 4.4.2 | Noise | 23 |
| 5 | Results and Discussion | 25 |
| 5.1 | Obtaining the Ground State Energy | 25 |
| 5.2 | Spin Gap | 29 |
| 5.3 | Singlet Pairing Correlation Functions for QLRO | 34 |

Contents

| | | |
|----------|--|-----------|
| 5.4 | Eigenvalue Analysis for QLRO | 40 |
| 5.5 | Sketch of the Phase Diagram for Two Different Fillings | 43 |
| 6 | Summary and Outlook | 47 |
| 7 | Appendix | 51 |
| 7.1 | Implementations | 51 |
| 7.2 | Lanczos Algorithm | 53 |
| 7.3 | Correlation Functions for 9 Stars | 55 |

1 Introduction

Understanding the behavior of materials at the quantum level is crucial for numerous applications in technology and science as condensed matter forms our daily lives. From devices we regularly use to materials shaping our environment, condensed matter physics comprises the modern world [GM14, cf. p. 5]. Quantum many-body systems show diverse physical phenomena and produce important macroscopic properties like high-temperature superconductivity (HTC) [Tim24]. HTC remains a widely pursued and intensively treated topic in current physical research [KKN⁺14], while its underlying mechanisms are not fully understood. Since the discovery of superconductivity at 30 K in 1986 in La-Ba-Cu-O ceramics [BM86], which exhibit superconductivity at considerably higher temperatures compared to those explained by BCS theory [Mou04], a lot of scientific research is dedicated towards uncovering the phenomenon of HTC [Mou04]. The role of electron correlations and lattice geometry are of interest concerning explanations for the superconducting nature of materials such as LSCO and YBCO [MSF⁺14]. The study of geometrically frustrated lattices emerged as a point of interest, because they can exhibit a macroscopic degeneracy of configurations hosting new physics [Sch24], [HHC⁺12]. For instance, the kagome lattice, which is realized in various minerals, e.g., herbertsmithite ($\text{ZnCu}_3(\text{OH})_6\text{Cl}_2$), is of interest with the hope to explore unconventional superconducting mechanisms [YYWW24], like the formation of Cooper-pair "molecules", which was published in 2024 in ref. [GWX⁺24]. This lattice is of significant interest in current research, such as in the study of kagome lattice metals like FeGe [TCY⁺22] and the recent claims of conventional superconductivity in doped kagome superconductors [XCW⁺24]. Researchers aim to understand and explain these kagome materials, e.g. by investigating the interplay between charge order and superconductivity using the Hubbard model, as discussed in ref. [NDY⁺22], particularly in compounds known as AV_3Sb_5 , where $A = \text{K}, \text{Cs}, \text{Rb}$. The aspects of frustration are particularly interesting in combination with strong electron correlations, for example in the context of

1 Introduction

the t - J model [ZR88], which is a simplification of the Hubbard model as one of the models for the theoretical description of high- T_C superconductors [MMM11] (see e.g. [Bol21] for a derivation). Due to a competition of a kinetic energy term and a spin exchange term, rich phase diagrams, including superconducting phases, result, see e.g., [OLSA91] and [MMM11] for a chain geometry.

This thesis focuses on the ground state phases of the t - J model on kagome strips, which are quasi-1D slices of the kagome lattice and thus it is expected to also show a rich phase diagram as already shown for a 1D system by [OLSA91]. We aim to characterize the phases such as the spin gap region and investigate the kagome strips in a similar way as to the chain geometry in ref. [MMM11] focusing on correlation functions and concepts like quasi-long-range order to identify a superconducting phase. This research is meaningful because understanding ground state properties of the t - J model on peculiar lattices like kagome strips, can help to better understand the broad problem of HTC depending on the role and interplay of strong electron correlation and frustration induced by the kagome lattice geometry.

The treatment of topics in quantum many-body physics, such as the investigation of superconductivity, is difficult and even numerical approaches trying to solve these problems become increasingly challenging: Consider a system of L spins, pointing either *up* or *down*. The dimension of the Hilbert Space \mathcal{H} grows exponentially with 2^L [Isi25]. The diagonalization of the Hamiltonian \hat{H} living on \mathcal{H} overwhelms conventional computational resources even for relatively small systems: e.g. ten spin-1/2 particles will lead to a matrix dimension of $2^{10} = 1024$. Thus, it is essential to implement effective algorithms to compensate for too little memory.

Obtaining sensible results is challenging because of the complexity of the kagome lattice. We simulate the t - J model on a kagome strip and try to characterize the phases of the ground state at low fillings ($n = 1/3$). Chapter 2 explains the underlying mathematical tools to characterize different phases of the t - J model on kagome strips. The kagome strip with its challenges is introduced in chapter 3. To realize computations with large system sizes, matrix product states and the density matrix renormalization group [WS98] are used, which are introduced in chapter 4. In chapter 5 the results for the characterized phases are presented, followed by a summary and an outlook for improvements and further research in this topic in chapter 6.

2 Theory

2.1 Quantum Many-Body Systems

A quantum system of $N \geq 1$ particles on a lattice at temperature $T = 0$ is described by the state vector $|\psi\rangle \in \mathcal{H}$, with \mathcal{H} the Hilbert space of the system with L lattice sites. The energy and state of this quantum system are determined by the time-independent *Schrödinger Equation* [Gri05, p. 21] with the Hamiltonian $\hat{H} : \mathcal{H}^L \rightarrow \mathcal{H}^L$

$$\hat{H} |\psi_n\rangle = E_n |\psi_n\rangle, \quad (2.1)$$

which is an eigenvalue problem with eigenvalues as energies. The smallest eigenvalue of Equation 2.1 is the ground state energy E_0 to the ground state vector $|\psi_0\rangle$. These problems in Quantum Many-Body Physics are notoriously hard to solve analytically [And05]. To gain insights into the properties of a system, observables are computed. The expectation value of an observable \hat{O} is defined as [Fli18]

$$\langle \hat{O} \rangle = \langle \psi | \hat{O} | \psi \rangle. \quad (2.2)$$

Observables \hat{O} are self-adjoint operators on a separable complex Hilbert space \mathcal{H} and thus Equation 2.2 yields a real-valued expectation value of \hat{O} (eigenvalue if $|\psi\rangle$ is an eigenstate of \hat{O}). For example, if the observable \hat{O} represents the position of a particle, the expectation value calculated from the state vector $|\psi\rangle$ gives the average position of the particle. If $|\psi\rangle$ is an eigenstate of \hat{O} , the expectation value yields the exact position of the particle.

In this work the ground state $|\psi_0\rangle$ with energy E_0 is computed to calculate expectation values of specific observables thereby investigating properties of the system.

2 Theory

Examples of observables relevant for this thesis are the total number operator

$$\hat{N} = \sum_{j,\sigma} \hat{n}_{j,\sigma}$$

and the total z-component of the spin

$$\hat{S}_z = \sum_j \frac{1}{2} (\hat{n}_{j,\uparrow} - \hat{n}_{j,\downarrow}).$$

$\hat{n}_{j,\sigma}$ with $\sigma = \uparrow, \downarrow$ is given by $\hat{n}_{j,\sigma} = \hat{c}_{j,\sigma}^\dagger \hat{c}_{j,\sigma}$ with $\hat{c}_{j,\sigma}^\dagger, \hat{c}_{j,\sigma}$ as the creation and annihilation operators for an electron with spin σ on lattice site j , respectively, satisfying [CTDL07, cf. p. 458]

$$\{\hat{c}_{i,\sigma}^\dagger, \hat{c}_{j,\sigma'}\} = \delta_{ij} \delta_{\sigma\sigma'}. \quad (2.3)$$

Later, the fermionic creation and annihilation operators $\hat{f}_{j,\sigma}^\dagger, \hat{f}_{j,\sigma}$ that project out double occupied sites are used.

2.2 Phases and Phase Transitions

Phases are distinct states of matter that are constituted by the microscopic description of the system like solid, liquid or gaseous. In the case of water, the phases are defined using thermodynamic properties like temperature, pressure, volume, number of particles, entropy, and chemical potential [Köh19]. To understand and characterize phases, which are explored in this thesis, order parameter and symmetry breaking are introduced.

2.2.1 Order Parameters and Symmetry Breaking

Phases are distinguished from each other by their order parameter that can be used to describe a phase transition of a system. In the ordered phase, the order parameter usually has a non-zero value, but it becomes zero in the disordered phase after a phase transition where a change of physical properties occurs [Ess]. Phase transitions such as those of water are driven by thermal fluctuations. Quantum phase

transitions occur at zero temperature $T = 0$, are driven by quantum fluctuations and in our work are characterized by changes of the ground state. The phase transition occurs at the quantum critical point, as discussed in [Köh19] and [BRvW19], with this thesis mainly exploring a superconducting phase [MMM11].

The expectation value of the order parameter is used to distinguish between symmetry-breaking states [BRvW19]. Beekmann et al. [BRvW19] state that ideally this expectation value should be zero in any symmetric state and otherwise an unique non-zero value.

The following introduction focuses on the aspects explained in ref. [BRvW19]. In Landau's theory of phase transitions, the formation of a finite order parameter is the consequence of spontaneous symmetry breaking (SSB). Systems undergoing SSB have degenerate ground states and while the Hamiltonian \hat{H} is symmetric, the ground states are not necessarily. Mathematically, this means a state $|\psi\rangle$ is not symmetric under a transformation \hat{U} , but $[\hat{H}, \hat{U}] = 0$. Since \hat{H} , \hat{U} commute, $|\psi\rangle$ and $\hat{U}|\psi\rangle$ must have the same eigenvalue and thus many different states $|\psi\rangle$, $\hat{U}|\psi\rangle$, $\hat{U}'|\psi\rangle$, \dots have the same energy. The system cannot be in all states simultaneously so it chooses one ground state, which breaks the symmetry. The order parameter \mathcal{O} is then defined as the operator whose eigenstates are the inequivalent states, with different and non-zero eigenvalues for each of these states. A detailed explanation for constructing an order parameter can be found in ref. [BRvW19]. Regardless, nearly always the physics of the observed system suggests an order parameter. For example: The Quantum Ising Model with a transversal magnetic field suggests the magnetization as an order parameter. However, in general $[H, \mathcal{O}] \neq 0$, meaning an eigenstate $|\psi\rangle$ of \hat{H} is not an eigenstate of \mathcal{O} as well as resulting in

$$\langle\psi_0|\mathcal{O}|\psi_0\rangle = 0 \quad (2.4)$$

for all finite system sizes. In the thermodynamic limit $N \rightarrow \infty$, we get $\langle[H, \mathcal{O}]\rangle = 0$ and the states that break the symmetry are eigenstates of \hat{H} . It follows

$$\langle\mathcal{O}\rangle = \lim_{h \rightarrow 0} \lim_{N \rightarrow \infty} \langle\psi_0(h, N)|\mathcal{O}|\psi_0(h, N)\rangle \quad (2.5)$$

with $|\psi_0(h, N)\rangle$ as the ground state of a system with N spins under a small field h , which depends on the investigated problem.

The emergence of a finite order parameter through SSB has its limitations in low-dimensional systems. According to the *Hohenberg-Mermin-Wagner theorem*, in one- and two-dimensional systems with continuous symmetries, thermal fluctuations at finite temperatures prevent the occurrence of SSB [MW66], [Hoh67] and quantum fluctuations in 1D ($T = 0$) and hence the expectation value in Equation 2.5 vanishes. In order to still characterize phases in such systems, the concepts long-range order (LRO) and quasi long-range order (QLRO) are introduced, which can be identified by analyzing the behavior of correlation functions.

2.2.2 Long-Range Order and Quasi Long-Range Order

The following section is mainly based on the descriptions in [Pae20]. Long-range correlations in the system can be used to distinguish phases. According to the *cluster decompositions theorem* [SW78] the correlation function between two local observables \hat{X}_i, \hat{Y}_j is 0 for infinitely large distance $|i - j|$

$$\lim_{|i-j| \rightarrow \infty} \langle \hat{X}_i \hat{Y}_j \rangle - \langle \hat{X}_i \rangle \langle \hat{Y}_j \rangle = 0. \quad (2.6)$$

Now consider $\hat{X}_i = \hat{Y}_i$, then we can write

$$\lim_{|i-j| \rightarrow \infty} \langle \hat{O}_i \hat{O}_j \rangle = O^2 \neq 0, \quad (2.7)$$

for $\hat{X}_i = \hat{O}_i$ as an order parameter with $\hat{O} = \frac{1}{N} \sum_j \hat{O}_j$. The correlation function in Equation 2.7 will provide properties of the order parameter since it yields a finite value $\langle \hat{O}_j \rangle \equiv O$ in an ordered phase with $\langle O \rangle \neq 0$. In the thermodynamic limit, an ordered phase will have a finite value for $|i - j| \rightarrow \infty$, whereas, in a disordered phase, correlations decay exponentially to zero:

$$C_{ij} \propto \begin{cases} \text{constant} & \text{if long-range ordered} \\ e^{-|i-j|/\xi} & \text{if disordered.} \end{cases}$$

Therefore, due to the difficulties explained in the previous section for finite systems, we cannot use equation 2.5 to analyze the order parameter, but instead, we can observe the behavior of correlation functions to detect symmetry breaking [PO56],

[Yan62]. There are various correlation functions which can indicate the presence of distinct phases. An example is given by $\hat{X}_j = \Delta_i^\dagger$ and $\hat{Y}_j = \Delta_j$, where

$$\Delta_i^\dagger = \frac{1}{\sqrt{2}} \left(c_{\downarrow, i_1}^\dagger c_{\uparrow, i_2}^\dagger - c_{\uparrow, i_1}^\dagger c_{\downarrow, i_2}^\dagger \right) \quad (2.8)$$

is the singlet pairing operator [MMM11] with $f_{i,\sigma}^\dagger$, $f_{i,\sigma}$ as the fermionic creation and annihilation operators at site i_1 (or i_2) with spin orientation σ . This leads to the formulation of the singlet pairing correlation function

$$P_{ij} = \langle \Delta_i^\dagger \Delta_j \rangle \quad (2.9)$$

which can be investigated similarly to the calculations in [Pae20]. For a small system instead of taking $|i - j| \rightarrow \infty$ we diagonalize the hermitian matrix P_{ij} which yields real eigenvalues λ_ν and eigenvectors v_ν and we can write

$$P_{ij} = \sum_\nu v_\nu^* \left(\langle \psi | \sum_i v_{\nu,i}^* \hat{a}_i^\dagger \right) \left(\sum_i v_{\nu,j} \hat{a}_i | \psi \rangle \right) v_\nu,$$

with eigenvalues $\lambda_\nu \geq 0$. Applying the *cluster decomposition theorem* shows

$$\lim_{|i-j| \rightarrow \infty} P_{ij} = \lim_{|i-j| \rightarrow \infty} \sum_\nu \nu_i \left\langle \psi \left| \sum_k \nu_{\nu,k}^* \Delta_k^\dagger \right| \psi \right\rangle \underbrace{\left\langle \psi \left| \sum_l \nu_{\nu,l} \Delta_l \right| \psi \right\rangle}_{=\sqrt{\lambda_{\max}}} \nu_{\nu,j}^\dagger \stackrel{!}{=} \lim_{|i-j| \rightarrow \infty} \langle \Delta_i^\dagger \rangle \langle \Delta_j \rangle,$$

where the last equality can only be true if there is exactly one eigenvalue $\lambda_\nu = \lambda_{\max}$, which is not vanishing. Additionally, we see that $\langle \Delta_j \rangle = \sqrt{\lambda_{\max}}$. In finite systems, these exact relationships may not apply. However, as the system size increases, a dominant eigenvalue tends to emerge. Therefore, for large systems, the behavior can be approximated by

$$\lim_{|i-j| \rightarrow \infty} P_{ij} \approx \lambda_{\max} v_{L,i} v_{L,j}^*.$$

The dominant eigenvalue scales with the system size $\lambda_L \sim L$ because the coefficients of the eigenvectors scale with $\sim \frac{1}{\sqrt{L}}$.

It is also possible for a correlation function C_{ij} to decay algebraically, $C_{ij} \propto |i - j|^c$. This case is referred to as quasi-long-range order because $\langle \mathcal{O} \rangle = 0$ in the thermodynamic limit. This can occur at low dimensional systems according to the *Hohenberg-Mermin-Wagner theorem* because SSB of a continuous symmetry cannot be realized [MW66] [Hoh67]. Therefore, the discussion about superconductivity (see section 2.2.3), which is a key phase we are investigating in this thesis, may only exhibit quasi-long-range order, as we will see in section 5.3. Mapping two-dimensional classical systems onto one-dimensional quantum systems at $T = 0$ shows that superconductivity cannot appear in one dimension at $T = 0$ [Sac11], [Aue94]. This means the values are finite except for $|i - j| \rightarrow \infty$, indicating a lack of true long-range order. A phase is then characterized by the correlation function which decays slowest.

2.2.3 BCS Theory and Superconductivity

Superconductors are materials exhibiting specific physical properties such as a vanishing electrical resistance and expulsion of magnetic fields from the material. In contrast to ordinary metallic conductors, superconductors have a characteristic critical temperature below which the electrical resistance discontinuously drops to zero. The Bardeen-Cooper-Schrieffer (BCS) theory explains the microscopic mechanism of superconductivity by condensation of Cooper pairs (pairs of electrons) [Com22, cf. p. 1-16]. Electrons near the Fermi surface form Cooper pairs through an attractive potential due to phonons, which are bosons [GM14, p. 775]. At low temperatures T , these can form a macroscopic quantum state known as a Bose-Einstein condensate. This condensation results in a collective state that increases the energy barrier required to disrupt any single electron pair or affect the entire condensate. Therefore it enables the superconductor to carry current without resistance [GM14, p. 775f.]. A more detailed description of BCS theory and superconductivity as a whole can be found in [Com22]. High Temperature Superconductors (HTC) are particularly interesting since they can be cooled with liquid nitrogen, which has a boiling point of 77 K. HTCs can achieve superconductivity at relatively high temperatures, whereas previously known superconductors required cooling with helium. Other than BCS-type superconductivity, the mechanism in HTC is widely unknown. It is hypothesized that spin fluctuations, rather than phonons, play a key role in HTC.

One way to identify superconductivity is by examining the singlet correlation function for pairing operators (Eq. 2.9) which has been shown exemplary in the previous chapter. To analyze the correlation matrix P , we diagonalize it and extract eigenvalues. If one eigenvalue λ_1 is significantly larger than the others ($\lambda_1 \gg \lambda_2, \lambda_3, \dots$), long-range order in the system is indicated. The largest eigenvalue λ_1 signifies a macroscopic occupation of the corresponding eigenvector state [PO56].

Only tendencies for a dominant eigenvalue are expected because of the *Hohenberg-Mermin-Wagner theorem*. Quasi long-range order can be observed and thus an indication for a superconducting phase is not exclusively given for the eigenvalue-relationship. When plotting the correlation functions over the distance, the decay needs to be evaluated. In view of phase transitions, different correlation functions can be compared as an indication of the dominant phase characterized by the smaller decay. In this thesis, a comparison of the spin-spin correlation function $S_{ij} = \langle S_z^i S_z^j \rangle$, the density-density correlation function $N_{ij} = \langle n_i n_j \rangle - \langle n_i \rangle \langle n_j \rangle$ and the singlet pairing correlation function $P_{ij} = \langle \Delta_i^\dagger \Delta_j \rangle$ can provide insights about the presence of a superconducting phase. Especially if the correlation functions show an equal exponent (for algebraic decay) for a special parameter combination, it can indicate a change of phases.

3 Modeling

This chapter will provide information about the model and the treated lattice structure. The investigated lattice is a quasi-1D system and therefore suited for DMRG (see chapter 4). The *Hohenberg-Mermin-Wagner theorem* applies and thus no true long-range order can be obtained as we will see in chapter 5.3.

3.1 The t - J Model

The t - J model serves as a theoretical approach to understanding high temperature superconductivity in cuprate superconductors, which develop from doped antiferromagnets. The t - J model describes conduction electrons (or holes) migrating between lattice sites and includes strong electron correlation, characterized by mutual Coulomb repulsion. Thus, electrons are highly unlikely to occupy the same site. The t - J model describes conduction electrons (or holes) migrating between lattice sites and includes strong electron correlation, which is characterized by mutual Coulomb repulsion. This leads to the situation that electrons are highly unlikely to occupy the same site. The Hamiltonian of the t - J model, which can be derived from the Hubbard model (see for example [Bol21]), is given by [MMM11]

$$\hat{H} = -t \sum_{\langle i,j \rangle, \sigma} \left(\hat{f}_{i,\sigma}^\dagger \hat{f}_{j,\sigma} + \text{H.c.} \right) + J \sum_{\langle i,j \rangle} \left(\vec{S}_i \cdot \vec{S}_j - \frac{1}{4} \hat{n}_i \hat{n}_j \right), \quad (3.1)$$

where the first term is the kinetic energy, the second term is the spin exchange interaction and the third term a density interaction term. The operators $\hat{f}_{i,\sigma}^\dagger, \hat{f}_{i,\sigma}$ are the fermionic creation and annihilation operators at site i with spin orientation σ (see section 2.1) which project out doubly occupied sites $\{\uparrow\downarrow\}$. The density operator is defined as $n_i = \hat{f}_{i,\sigma}^\dagger \hat{f}_{i,\sigma}$ and the spin operator as $S_i = \hat{f}_{i,\alpha}^\dagger \vec{\sigma}_{\alpha\beta} \hat{f}_{i,\beta}$, where $\vec{\sigma}_{\alpha\beta}$ represents the components of the Pauli matrices. The parameter t determines hopping strength

3 Modeling

and J the strength of the interaction term. The basis of the t - J model is given by $\{|0\rangle, |\uparrow\rangle, |\downarrow\rangle\}$, where $|0\rangle$ indicates a site without an electron, and $|\uparrow\rangle, |\downarrow\rangle$ a site with an electron with *up/down* spin.

For a chain, there are different phases depicted in Figure 3.1. The figure shows a metallic phase (M), a gapless superconducting phase (SC), a singlet-superconducting phase with spin gap (SG + SS) and phase separation (PS) for which the system separates into a hole-rich and an electron-rich part. The energy gap is given by

$$\Delta_S = E_0(N, S_z^{\text{tot}} = 1) - E_0(N, S_z^{\text{tot}} = 0) \quad (3.2)$$

to triplet excitations (spin gap), and the density-density correlation functions

$$N_{ij} = \langle n_i n_j \rangle - \langle n_i \rangle \langle n_j \rangle \quad (3.3)$$

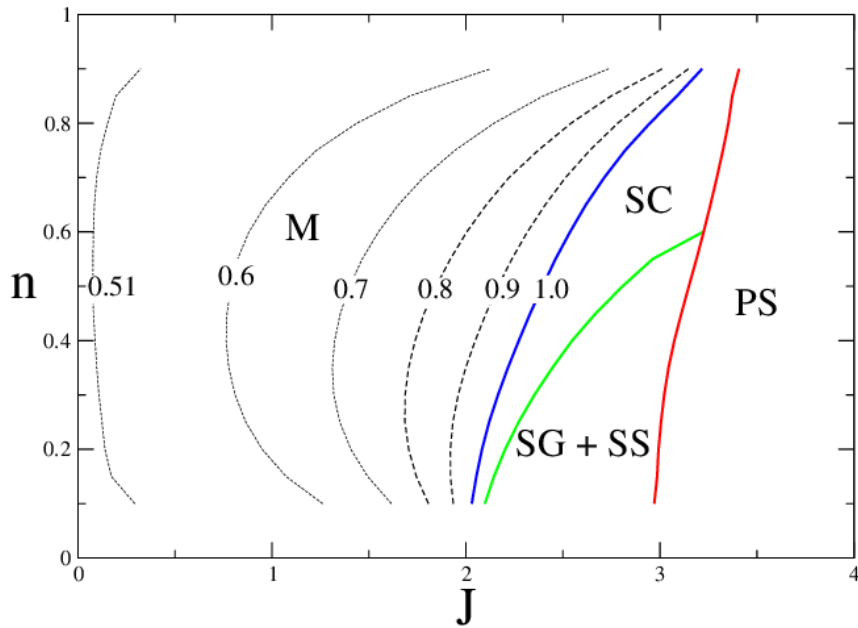


Figure 3.1: Phase diagram of the 1D t - J model for densities $0.1 \leq n \leq 0.9$ and in the range $0 < J \leq 4$ with $t = 1$. This diagram is obtained by DMRG (see chapter 4.1). $n = N/L$ represents the electronic density, where N is the total number of particles and L the number of lattice sites. The symbols mean: metallic phase (M), superconducting phase (SC), phase separation (PS) and singlet-superconducting phase with spin gap (SG + SS) [MMM11].

can be used to compute the different phases [MMM11]. Consider a half-occupied system $n = 0.5$. For $J/t = J \gg 1$, the hopping term is suppressed. Therefore, phase separation is observed meaning, distinct islands of spins that do not move anymore. The formation of localized "islands" is caused by the minimization of the energy by aligning the spins in a way that maximizes the exchange interaction. However, if J is smaller than 1, respectively t , a metallic phase is more favorable. This is because the kinetic energy term dominates, promoting the delocalization of spins and allowing them to move freely. Right between these phases, we can observe the superconducting phase.

3.2 Kagome Geometry

The chain serves as an orientation for the investigated phase diagram in this thesis. Theoretically speaking, it should be possible to create such a phase diagram for any graph $G = (V, E)$ which consists of sites and connections between them. To introduce the kagome lattice and highlight its significance and peculiarity, we consider a triangular lattice as an antiferromagnetic model, as shown in Figure 3.2: If the spin on the left corner is $+1$ and the spin on the top is -1 , we cannot assign the third spin to a correct value of ± 1 since this frustrates at least one of the existing spins.

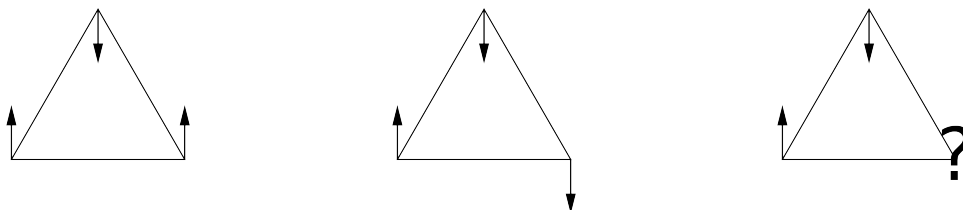


Figure 3.2: Triangle with three spins pointing either up or down and antiferromagnetic exchange interaction between them. Spin *up* frustrates the top and spin *down* frustrates the left corner.

This phenomenon of frustration is relevant for the kagome geometry as shown in Figure 3.3. The geometrically frustrated lattice is made up of corner-sharing triangles. As can be observed in Figure 3.2: Two spins can be antiparallel, however, the third one is frustrated for both of the other configurations. The frustration

leads to a degeneracy of configurations which can result in a spin liquid [And87], [HHC⁺12]. Concretely, we have a system with a disordered spin distribution even at temperatures $T \rightarrow 0$.

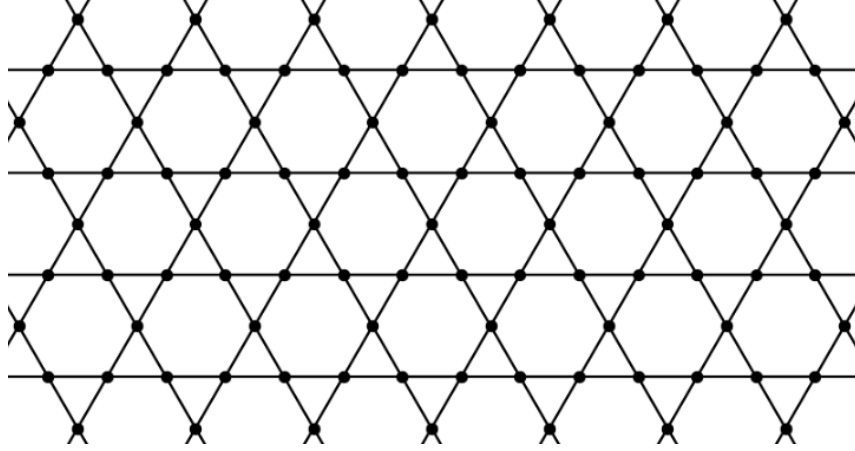


Figure 3.3: 2D kagome lattice consisting of corner-sharing triangles and thus being highly frustrated.

3.3 Kagome Strip

The ground state properties will be investigated for the strip depicted in 3.4 which is a quasi-1D system. The lattice has $L = 8 + 7 \cdot (n - 1)$ sites with n as the number of stars because every star (red in Figure 3.4) consists of 8 sites but has one overlap with the next star.

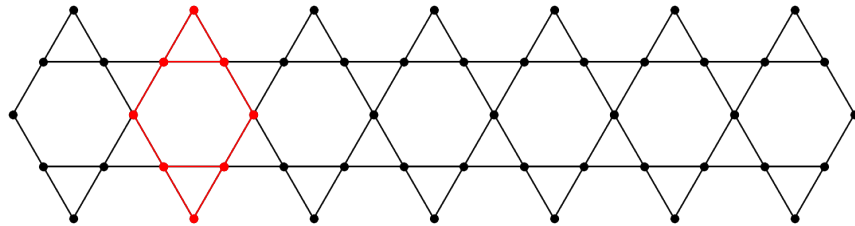


Figure 3.4: Visualization of kagome strip that will be used. This is one strip of the two-dimensional kagome lattice in Figure 3.3, with one star colored red.

The multiples of stars as the number of sites hampers the treatment of the system immensely because comparison for arbitrary system sizes is not possible. To create a phase diagram similar to Fig. 3.1, different fillings n need to be considered, however, finding common divisors is not trivial. For example: The two systems consisting of

5 and 7 stars have 36 and 50 sites and thus can only be divided by 2. Here, we want to stay at fillings $n \leq 1/2$ since $n = 1/2$ has the largest number of configurations and consequently the highest computational effort. This is because the number of possible configurations is given by $\binom{n}{k}$ which is maximized for $k = n/2$ (can be proven by induction).

3.3.1 Mapping of the Lattice

For a chain, iterating over sites i and $i + 1$ in the t - J model Hamiltonian in Eq. 3.1 defines the neighbors $\langle i, j \rangle$. On the other hand, for a kagome strip it is possible for i to have several neighbors j and their indices might not be nearest neighbors. In general, indexing the sites of the kagome strip is arbitrary and there are several possible numerations to choose from. This numeration is then mapped to a chain and thus defines interactions between indices. Subsequently, this can be used to implement the Hamiltonian in accordance to Eq. 3.1. However, as can be seen in Figure 3.5, one cannot avoid to have indices that interact with farther sites on the chain.

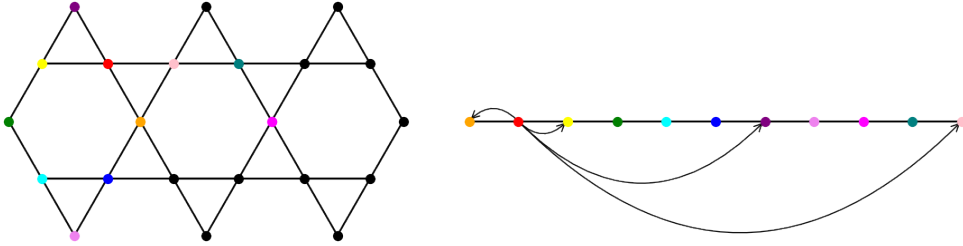


Figure 3.5: Visualization of the mapping from kagome strip to chain. Long-distance bonds are associated with large entanglement, which is problematic for the DMRG algorithm (see section 4.4).

This enlarges the entanglement which makes it numerically expensive to converge to the ground state with DMRG as we will see in the next chapter. The entanglement between parts of the geometry determines the bond dimension of the MPS (see section 4.1). If we map the nearest neighbors to distant sites on a chain (their indices), the complexity of the entanglement increases, requiring a larger bond dimension [PKS⁺19].

A possibility to fight the entanglement would be to reduce to complexity of the index-basis. Concretely, we want to achieve the objective of minimizing the sum

of the distances between adjacent sites in the linear arrangement and minimizing the maximum distance between any sites. This problem is related to the Minimum Linear Arrangement problem which is NP-hard [ABCF17]. Consequently, it cannot be solved exactly for large lattices. Hence we are just focusing on finding a sensible indexing of the vertices.

3.3.2 Definition of Distance

In contrast to the chain, how to measure the distance in a kagome strip is a bit more complicated. In order to be able to investigate LRO/QLRO in the kagome strip, we need to investigate a correlation matrix C_{ij} contingent on the distance $|i - j|$ of the respective sites. Here, we take a simple choice: As illustrated in Figure 3.5, a distance can be defined by considering the red upper or lower chains which the kagome strip partly consists of. Since the problem is (if converged) symmetric, we can choose one of the lines and chose the upper one.

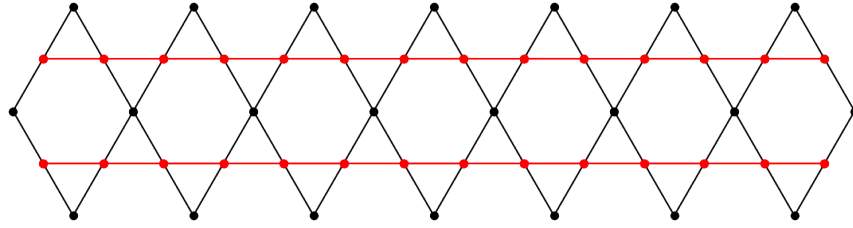


Figure 3.6: Kagome strip with two red chains. The red lines represent the indices and bonds which can be used to plot correlations over a distance $|i - j|$.

Depending on the specific value $|i - j|$, there might exist more than one arrangement. In order to minimize boundary effects, the average of the values of C_{ij} for a value of $|i - j|$ is taken. To minimize boundary effects, it is also sensible to exclude configurations that include sites at the very boundaries.

3.3.3 Definition of Bonds

Not only the sites, but also the edges E of the graph of the kagome strip are numbered. An example for a correlation between two bonds is depicted in Figure 3.7 in red color.

The number of bonds is given by $b = 10 + 12(n - 1)$ with n as the number of stars. Each entry of the correlation matrix

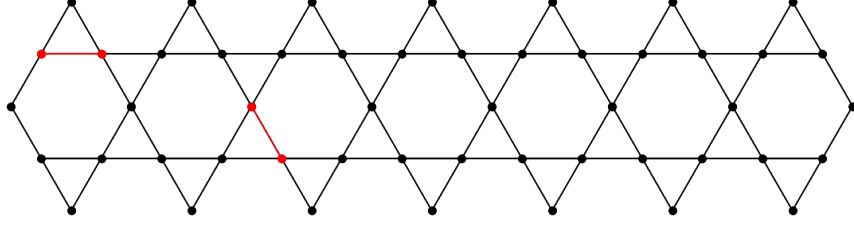


Figure 3.7: Kagome strip with two red bonds. These are two example bonds whose correlation is an entry in a correlation matrix.

$$P_{ij} = \langle \Delta_i^\dagger \Delta_j \rangle$$

is a correlation between two bonds i, j of the kagome strip. In general, we obtain four terms (ITensor implementation in the appendix in section 7.1)

$$\begin{aligned} \langle \Delta_i^\dagger \Delta_j \rangle = \frac{1}{2} & \langle f_{\uparrow, i_1}^\dagger f_{\downarrow, i_2}^\dagger f_{\uparrow, j_1} f_{\downarrow, j_2} - f_{\uparrow, i_1}^\dagger f_{\downarrow, i_2}^\dagger f_{\downarrow, j_1} f_{\uparrow, j_2} \\ & - f_{\downarrow, i_1}^\dagger f_{\uparrow, i_2}^\dagger f_{\uparrow, j_1} f_{\downarrow, j_2} + f_{\downarrow, i_1}^\dagger f_{\uparrow, i_2}^\dagger f_{\downarrow, j_1} f_{\uparrow, j_2} \rangle \end{aligned}$$

with i_1, i_2 being the sites of bond i and j_1, j_2 as the two sites of bond j . As introduced in section 3.1, the operators $f_{i, \sigma}^\dagger, f_{i, \sigma}$ are the fermionic creation and annihilation operators at site i with spin orientation σ which project out doubly occupied sites $\{\uparrow\downarrow\}$.

4 Numerical Methods

For the investigations pursued in this thesis, we need to compute the ground state vector $|\psi_0\rangle$ and energy E_0 of a quantum many-body system. The state vector $|\psi_0\rangle$ is required to compute the expectation values of observables $\langle\mathcal{O}\rangle$ of interest to gain insights into the phase diagram for the t - J model on kagome strips (see chapter 3). In this chapter, we introduce matrix product states (MPS), which provide a technique to represent and approximate a state $|\psi_0\rangle$. Additionally, we can compute expectation values $\langle\mathcal{O}\rangle$ using matrix product operators (MPO). Detailed descriptions can be found in reference [PKS⁺19].

4.1 Matrix Product States

A matrix product state is a representation of a quantum state of N particles on L sites

$$|\psi\rangle = \sum_{\sigma_1, \dots, \sigma_L} \sum_{m_0, \dots, m_L} T_{1; m_0 m_1}^{\sigma_1} \cdots T_{L; m_{L-1} m_L}^{\sigma_L} |\sigma_1, \dots, \sigma_L\rangle, \quad (4.1)$$

where T are rank-3 tensors. For each fixed value of σ_i , the tensor T is a matrix with entries labeled by m_{i-1} , m_i that describe the state locally. This makes it efficient when evaluating local observables. To better understand MPS, we examine them through the example of the t - J model: Consider the local basis states of the t - J model given by $|0\rangle$, $|\downarrow\rangle$ and $|\uparrow\rangle$ (see section 3.1). The dimension of the Hilbert space on a site is $d = 3$. For a quantum many-body system consisting of L sites, the complete basis is expressed by

$$|\sigma_1\rangle \otimes \cdots \otimes |\sigma_L\rangle = |\sigma_1, \dots, \sigma_L\rangle \quad (4.2)$$

with $1 \leq \sigma_i \leq d$ as one of the possible configurations on site i . Hence, a possible state $|\psi\rangle$ is given by a linear combination

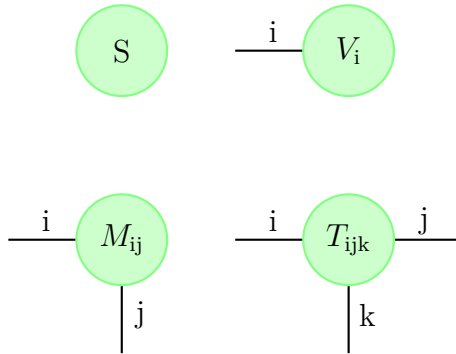
$$|\psi\rangle = \sum_i c_{\sigma_i} |\sigma_1, \dots, \sigma_L\rangle. \quad (4.3)$$

The underlying idea of MPS is that coefficients the c_{σ_i} from Equation 4.3 can be represented as a product of L rank-3 tensors (see Equation 4.1). The largest index for m_i is called bond dimension χ . A matrix product state can either be exactly represented when the bond dimension is not limited, or be approximated when restricting the bond dimension to an integer $n \in \mathbb{N}$. Higher entanglement of a system requires a larger bond dimension χ . The entanglement is minimized for one-dimensional systems that only exhibit nearest-neighbor interactions and grows on higher dimensions. The entanglement entropy scales with the boundary area (area law of entanglement [ECP10]). Therefore, it is expected that χ is larger for the kagome strip than for a chain geometry. The increased bond dimension for the kagome strip will lead to a higher computational cost expressed by longer runtimes and decreased accuracy compared to the chain.

So instead of saving all coefficients, matrices are stored that can be used to compute the coefficients. To get an entry $c_{\sigma_1, \dots, \sigma_L}$, one needs to contract T_i over their lower indices. However, in practice, this is not done, but the local representation is directly used to compute expectation values of local observables.

4.2 Tensor Networks

To understand MPS, we make use of tensor networks with a diagrammatic approach from [BK18] and [PKS⁺19].



Each node represents a tensor, which is multi-dimensional array of numbers. Each line that spreads apart from a node is an index. Hence a matrix is represented by a node with two leaving lines representing the two indices to define the entries in the matrix. Furthermore, a connection between two nodes describes a contraction over this index. This index is multiplied or summed over. The most prominent example of tensor network states are MPS [BK18], visualized in Figure 4.1.

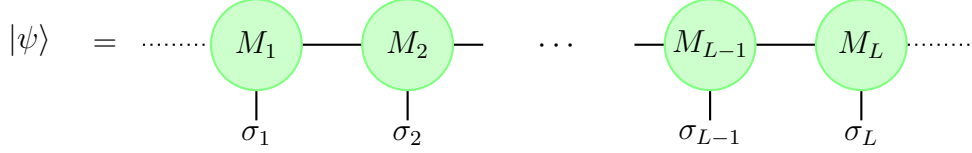


Figure 4.1: Tensor network representation of a matrix product state $|\psi\rangle$. The nodes M_1, M_2, M_{L-1} and M_L represent the rank-3 tensors from Equation 4.1.

4.3 Matrix Product Operators

Analogous to quantum states $|\psi\rangle$, every operator \hat{O} can be expressed as a matrix-product operator (MPO). A MPO is a contraction of L rank-4 tensors W_j

$$\hat{O} = \sum_{\substack{\sigma_1, \dots, \sigma_L \\ \sigma'_1, \dots, \sigma'_L}} c_{\sigma_1 \dots \sigma_L \sigma'_1 \dots \sigma'_L} |\sigma_1, \dots, \sigma_L\rangle \langle \sigma'_1, \dots, \sigma'_L| \quad (4.4)$$

$$= \sum_{\substack{\sigma_1, \dots, \sigma_L \\ \sigma'_1, \dots, \sigma'_L}} \sum_{w_0, \dots, w_L} W_{1; w_0 w_1}^{\sigma_1 \sigma'_1} \dots W_{L; w_{L-1} w_L}^{\sigma_L \sigma'_L} |\sigma_1, \dots, \sigma_L\rangle \langle \sigma'_1, \dots, \sigma'_L|. \quad (4.5)$$

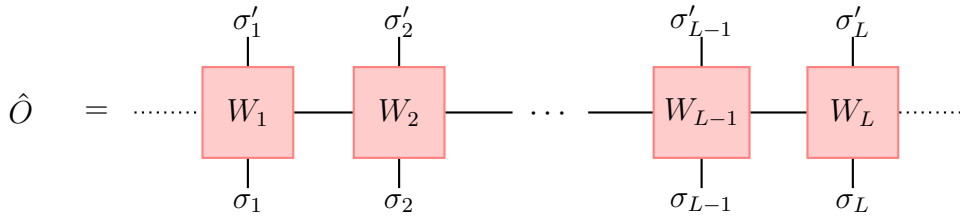


Figure 4.2: Tensor network representation of a matrix product operator \hat{O} . The nodes W_1, W_2, W_{L-1} and W_L represent the rank-4 tensors from Equation 4.5.

Similar to the quantum state, we can visualize the MPO with a tensor network representation. The MPO from Equation 4.5 is depicted in Figure 4.2. Combining the information from Figures 4.1 and 4.2 results in the expectation value $\langle \hat{O} \rangle$ of an operator \hat{O} . The resulting tensor network is illustrated in Figure 4.3. Since both, the matrices M and W are defined on each site, local expectation values can be computed using these local objects, so that one does not need the coefficients from Equation 4.3.

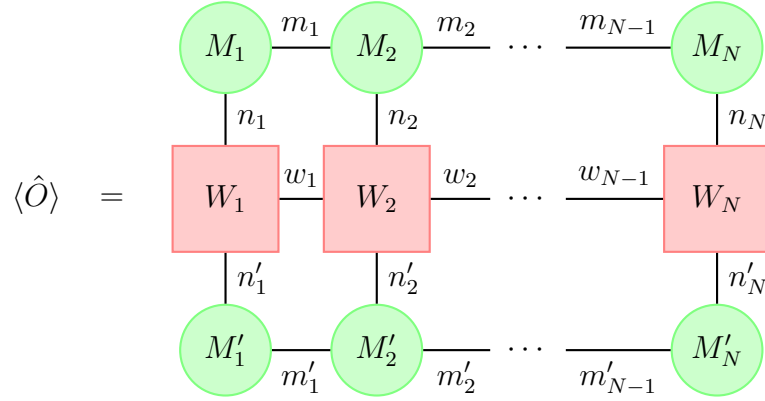


Figure 4.3: Tensor network representation for computing an expectation value with a MPS (see Fig. 4.1) and MPO (see Fig. 4.2). The ideal way of contraction order is sideways, e.g. from the left to the right [PKS⁺19].

4.4 Density Matrix Renormalization Group

The density matrix renormalization group (DMRG) is a numerical variational technique, which finds the smallest energy matrix product state vector $|\psi\rangle$ of a Hamiltonian \hat{H} . For one dimensional systems, DMRG is a highly efficient method. A detailed description can be found in [Köh19]. A brief version of the procedure is as follows: Start with an initial MPS guess for the ground state with a small bond dimension. Iteratively optimize one site at a time by sweeping along the lattice. The optimization of local tensors involves finding the ground state for the current step of the sweep, which is typically done using the Lanczos algorithm [Lan50], [Man22, cf. p. 212]. The algorithm provides an approximate ground state energy and the corresponding state vector in the Lanczos basis, which is then transformed back to the original Hilbert space (see section 7.2 in the appendix). After optimizing the local tensors, the bond dimension is truncated (see section 4.4.1). This process is

repeated, sweeping along the lattice to iteratively refine the ground state approximation. The number of sweeps n_{sweeps} and the maximum bond dimension χ_{max} need to be adjusted to fit the problem. In the next following two sections we want to explain the truncation and an essential implementation that we found to be necessary to obtain sensible ground states $|\psi_0\rangle$ and energies E_0 for the kagome strip.

4.4.1 Truncation

The basic idea of the method is the truncation of a matrix. Consider a matrix product state $|\psi\rangle$ with bond dimension χ . We want to find another state $|\psi'\rangle$ with bond dimension χ' and $\chi' \leq \chi$. This is done via Singular Value Decomposition [Sch11, cf. sec. 4.5] (SVD) on the bond tensors of the MPS by discarding small singular values. This leads to the definition of the discarded weight as the sum of the squares of the discarded singular values. Concretely, this means the matrices of the state $|\psi\rangle$ are approximated via SVD:

$$\sum_{s=1}^{\chi} U_{l,s} S_{s,s} V_{s,r}^{\dagger} \xrightarrow{\text{approximation}} \sum_{s=1}^{\chi'} U'_{l,s} S'_{s,s} V_{s,r}'^{\dagger}$$

where U and V^{\dagger} are unitary matrices and S is a diagonal matrix with non-negative entries, which are the singular values. The discarded weight is then given by

$$\sum_{k=\chi'+1}^{\chi} S_{k,k}^2, \quad (4.6)$$

where $S_{k,k}$ are the discarded singular values.

4.4.2 Noise

As already stated in chapter 3, kagome strips are subject to large entanglement. Since DMRG is a variational method, the ground state energy approximation can depend on the chosen initial state. We use ITensor [FWS22b] [FWS22a], where the initial state needs to be specified [CRI24], e.g., using the ITensor function `randomMPS(sites, state)`. This fills the matrices that compose the MPS with random values. The sites are defined via `siteinds("tJ", N; conserve_qns=true)`

specifying the investigated model, number of particles and ensuring the conservation of quantum numbers. Additionally, we need to guess an initial state. Since the ground state is expected to have no magnetization, we choose an initial state with $S_z^{\text{tot}} = 0$. This is achieved by defining the `state` with the identical number of *up* and *down* spins. In chapter 5 we explain that we use random initial state guesses that satisfy S_z^{tot} , i.e. a random distribution of spin *up/down* particles on the sites of the kagome strip (implementation in the appendix in section 7.1). The initial state guess is challenging, because the basis of the kagome strip is complicated (see section 3.3) since the algorithm gets stuck in local minima.

Getting stuck in local minima can be visualized by the following example: Consider the following potential landscape as shown in Figure 4.4.

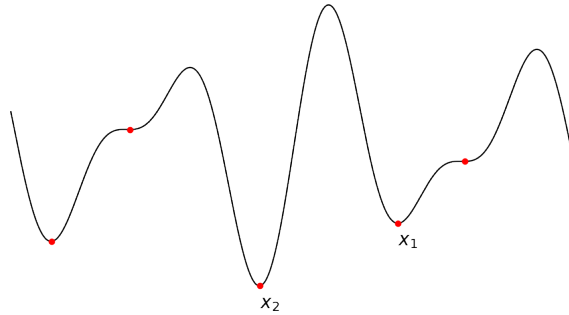


Figure 4.4: Potential landscape with several local minima. A local minimum cannot be distinguished from a global minimum locally.

We search for the global minimum, which is in this analogous example the ground state energy. When approaching a local minimum at x_1 and finding $f'(x_1) = 0$, x_1 might be mistaken as the global minimum x_2 . This can happen with the DMRG as well if the initial state and/or the optimization procedure are not suitable. Here we found the following solution: The implementation of a noise term can be helpful to avoid being stuck in local minima [CRI24]. The noise term is a small random perturbation added to the MPS. Concretely, a small number is added to the tensors of the matrix product state from Equation 4.1. This can move the state away from the local minimum and help to converge to the true ground state. However, unfortunately the noise term is not well explained in ITensor's documentation. In the next chapter we will see the consequences of this noise term. The noise term can be passed as a parameter array to the `dmrg` function `energy`, `psi = dmrg(H,psi0; nsweeps, maxdim, cutoff, noise)`.

5 Results and Discussion

This chapter presents the results for the properties of the t - J model on the kagome strip geometry introduced in section 3.3. The computations were mainly run with the Julia version of ITensor [FWS22b], [FWS22a]. The data analysis was performed using Python’s Pandas and Matplotlib libraries. Some important implementations, for example of the t - J Hamiltonian, can be found in the appendix in section 7.1. For comparison and sanity purposes, some of the results are also compared to the t - J chain reproducing the findings in [MMM11]. The ground state phases are investigated by examining different system sizes and varying the value of J/t . In the following, t is set to 1, which is why only the variation of J is of interest.

5.1 Obtaining the Ground State Energy

The first challenge is to accurately determine the ground state with its energy E_0 and state vector $|\psi_0\rangle$. As explained in the previous chapter, the system is subject to a huge entanglement. Although DMRG is very robust if the initial MPS is close to the ground state, in general, as for any variational method, there is not a guarantee of finding the true ground state. Matrix product states are analytically exact representations of quantum states (see section 4.1), but the truncation (see section 4.4.1) leads to an approximation. The accuracy of the DMRG sweeps can be characterized by the discarded weight (see section 4.4) which is desirable to converge at least to 1E-5, because otherwise the observables are not sufficiently accurate. Roughly speaking, a cutoff of 1E-5 results in sensible accuracy, 1E-8 in high accuracy and 1E-12 in near exact accuracy [Sto17].

We can support the statement that DMRG can give excellent results in as few as 4–5 sweeps [Sto17] for a chain geometry. For the kagome strips, however, 30 sweeps up to a bond dimension of 2000 are needed in order to get a small enough discarded weight

and thus have sufficient accuracy in the observables considered. The kagome strip as a quasi-two-dimensional system needs more sweeps and a larger bond dimension than the chain to yield representative results. If periodic boundary conditions (PBC) had been implemented, reaching convergence would have been more difficult. Although open boundary conditions (OBC) account for larger boundary effects, PBC will lead to a bigger entanglement, resulting in worse accuracy with significantly longer runtimes, and generally is more challenging for DMRG. However, it might be rational to pursue PBC's later on to better identify boundary effects.

For the kagome strip, we find that DMRG is prone to get stuck in local minima [CRI24], possibly because the initial state guesses were not optimal. This is not the case for a chain where the ground state energies are robust under random initial state guesses. Additionally, the runtime for the chain is substantially shorter. The energy E_0 for the kagome strip heavily depends on the chosen initial state MPS. This can be seen in table 5.1. A random initial state guess yields different energy results for a system consisting of 5 stars and a filling of $n = 1/3$. Interestingly, in each case DMRG "successfully" converged to a specific energy value E , since the energy difference between respective sweeps is of the magnitude of $10\text{E-}13$.

Table 5.1: Energy after 30 sweeps for each run for a system consisting of 5 stars and a filling of $n = 1/3$.

| Run | Energy After 30 Sweeps |
|-----|------------------------|
| 1 | -12.492110928924 |
| 2 | -18.309447920448 |
| 3 | -15.022868323657 |
| 4 | -17.666443289432 |
| 5 | -10.804193499928 |
| 6 | -10.903401015092 |

The energies in 5.1 are numerically stable but unquestionably not the true ground state values. The ground state can only be determined with numerical uncertainty. Thus, it is very important to perform a number of checks to ensure convergence. We find that the implementation of a noise term (see section 4.4.2) reduces the probability of convergence to local minima and is a possibility to obtain meaningful energies E_0 and states $|\psi_0\rangle$. In this case, the energy does not significantly change by varying the initial states and is robust when changing bond dimensions and number of sweeps. Implementing a noise term stabilizes the ground state energy which in

general is also significantly smaller than the previously computed values. However, the addition of a noise term is accompanied by longer computational runtimes. The accuracy of the ground state approximation heavily depends on the system size and filling. In Figure 5.1 we illustrate that the difference between consecutive sweeps of a 5 star kagome strip with filling $n = 1/6$ can be as low as $10\text{E-}13$ and have a discarded weight around $10\text{E-}12$, increasing the filling to $n = 1/3$ can lead to considerably worse accuracy.

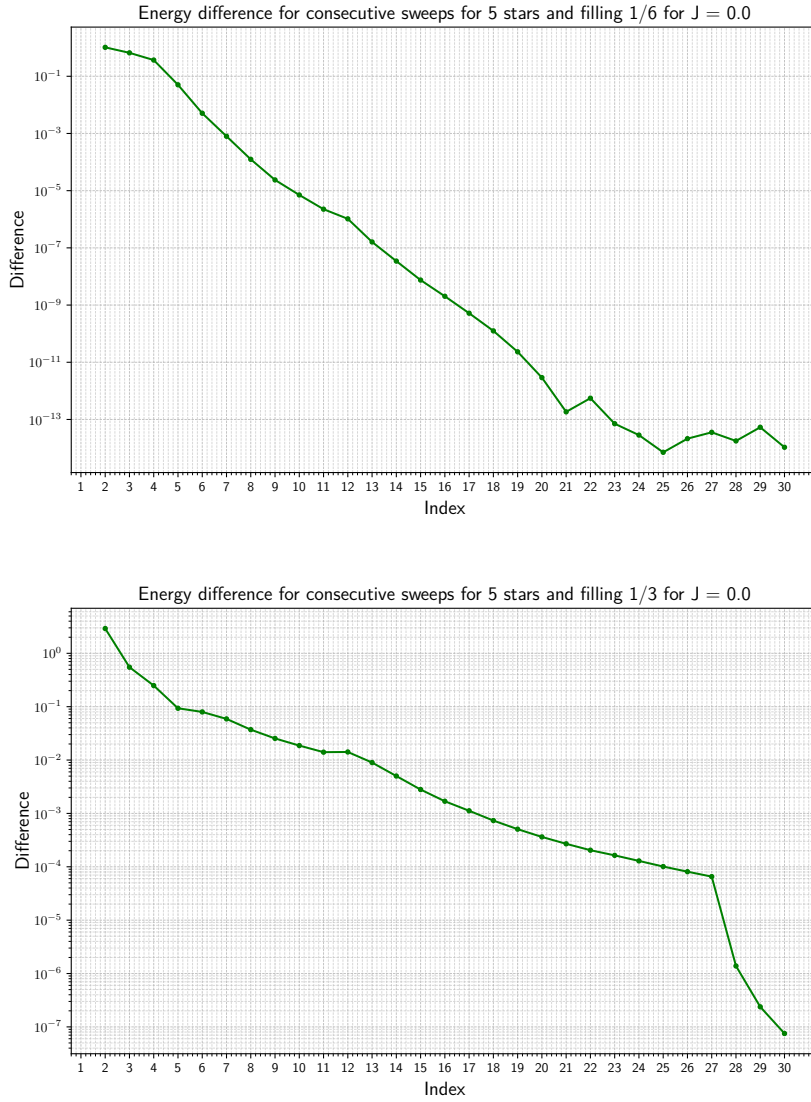


Figure 5.1: Energy difference between sweep $i + 1$ and i for a kagome strip consisting of 5 stars for $J = 0.0$ for filling $n = 1/6$ (top) and $n = 1/3$ (bottom) both with a noise term.

It is important to note that due to the increase in complexity, for a system consisting of 11 stars, the convergence generally takes longer. A suitable test to check whether the kagome strip system properly converged is to examine the local density distribution. It is expected to be symmetrical because, in the absence of SSB and at finite temperatures, local observables should respect the symmetries of the symmetric t - J Hamiltonian 3.1. In the thermodynamic limit and at zero temperature, spontaneous symmetry breaking can occur, which can lead to an asymmetric local density distribution even in a system with a symmetric Hamiltonian. As the thermodynamic limit is not reached, a symmetry should be evident for all local observables. The distribution is visualized in Figures 5.2 and 5.3. The local densities are obtained by computing the expectation value of the number operator with the ground state vector $\langle \hat{n}_i \rangle = \langle \psi_0 | \hat{n}_i | \psi_0 \rangle$. For the following plots, this value is scaled with a constant multiplier c and plotted as a circle with diameter $c \cdot \langle \hat{n}_i \rangle$ on the sites of the strip. Between 5 stars and 11 stars a different value for c is used for optimal visibility. The local densities look symmetrical for all $0.0 \leq J \leq 3.0$ with a smooth transition between the depicted figures for $J = 0.0$ and $J = 3.0$. For larger J the circles at the edges tend to get smaller indicating a smaller local density at the boundaries.

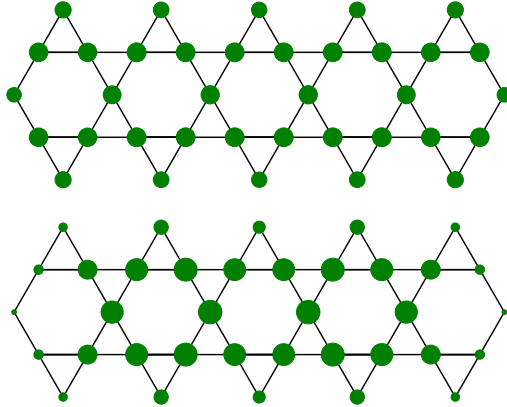


Figure 5.2: Local densities per site of a kagome strip consisting of 5 stars for $J = 0.0$ (top) and $J = 3.0$ (bottom). The density per lattice site is proportional to the diameter of the drawn circles. $\chi_{\max} = 2000$, $n_{\text{sweeps}} = 30$.

Although the figures seem to be perfectly symmetrical, $\langle \hat{n}_i \rangle$ needs to be checked in detail, because the accuracy of one observable \mathcal{O} , here \hat{H} , does not imply the equal accuracy for another observable \mathcal{O}' , here \hat{n}_i . For the case of the 5 star system, the symmetric sites show identical values for $\langle \hat{n}_i \rangle$ up to at least the 5th decimal place for $n = 1/3$. Decreasing the filling from $n = 1/3$ to, for instance, $n = 1/6$ leads

to an enhanced accuracy up to at least the 9th decimal. Moreover, a system of 11 stars also looks perfectly converged as depicted in Figure 5.3 for $J = 0.0$ and $J = 3.0$. However, the discarded weight for the ground state energy search is only around $10\text{E-}5$ and the $\langle \hat{n}_i \rangle$ values for symmetric sites are only accurate up to the 4th decimal. For the case of $J = 0.0$, the sites at the very boundaries on the left and right, are only accurate up to the 1st decimal.

The 5 and 11 star system with filling $n = 1/3$ are essential for the next chapter since they are the only appropriate system sizes at this filling amenable to the MPS within the limits of this work.

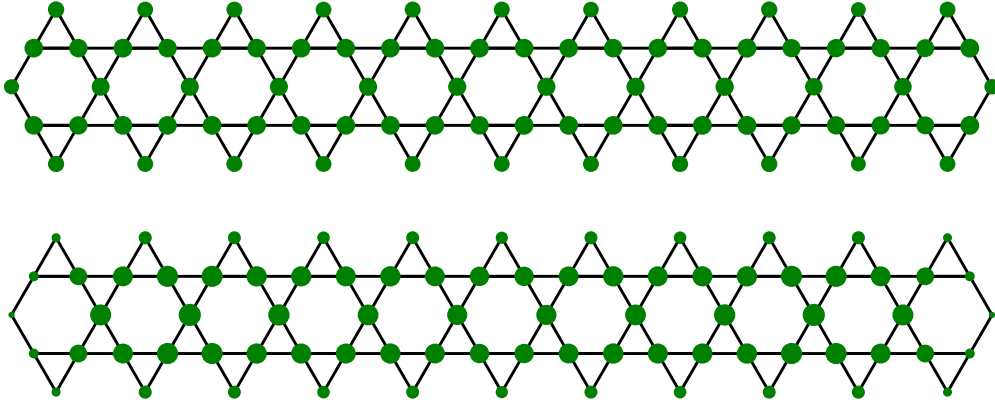


Figure 5.3: Local densities per site of a kagome strip consisting of 11 stars for $J = 0.0$ and $J = 3.0$. The density per lattice site is proportional to the diameter of the drawn circles. $\chi_{\max} = 2000$, $n_{\text{sweeps}} = 30$.

5.2 Spin Gap

Consider a system with ground state energy E_0 , then the spin gap value Δ_S is defined by Eq. 3.2 from section 3, i.e. the energy difference that occurs by flipping one *up/down* spin. In terms of the t - J model, it can be analyzed for which J values Δ_S is zero or finite. It is expected that the spin gap opens, meaning it becomes finite, at a certain value J_{crit} . In case of the chain, these spin gap values can be computed for various different system sizes. Here, 18, 36, 54, 66 and 78 sites are implemented, which are all divisible by 3. Moreover, a division by 3 yields an even number which is required to ensure $S_z^{\text{tot}} = 0$ before and $S_z^{\text{tot}} = 1$ after the spin-flip. We used $\chi_{\max} = 2000$, n_{sweeps} for the kagome strips and the chain.

When plotting the spin gap values, a linear trend becomes evident after the initial gap opens [ref. private communication with Karun Gadge]. This allows us to approximate the data using a linear regression model. The J values which are then obtained by the intersection of the regression with the x -axis (J -axis) are plotted over their inverse system size $1/L$. It is then possible to find the critical J_{crit} value for which the spin gap opens. The data for the spin gap values is depicted in Figure 5.4 for a filling of $n = 1/3$ and the plot of the J values over the inverse system size $1/L$ is illustrated in the inset plot of the same figure. The value is determined to be $J_{\text{crit}} = 2.25$ in the thermodynamic limit which approximately corresponds to the value reported in [MMM11] ($J_{\text{crit}} \approx 2.4$) and visualized in the phase diagram in Figure 3.1.

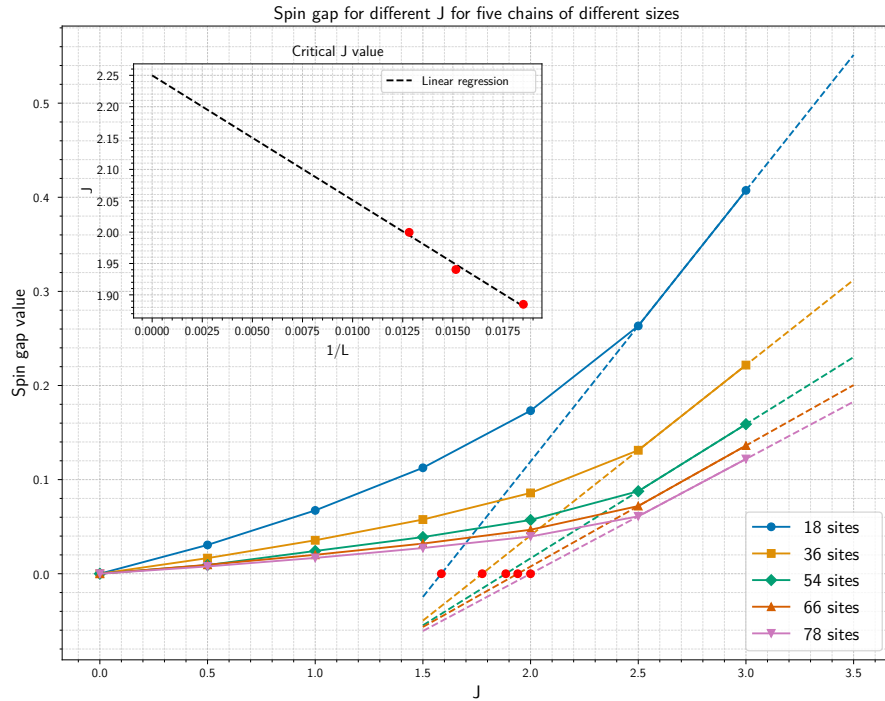


Figure 5.4: Spin gap value for 5 different chain sizes and different values of J between $0.0 \leq J \leq 3.0$ for a filling of $n = 1/3$. The spin gap opening is plotted over the inverse system size $1/L$ in the inset plot for the three largest systems. The critical value is $J_{\text{crit}} = 2.25$, which corresponds to the value reported in [MMM11]. $\chi_{\text{max}} = 2000$, $n_{\text{sweeps}} = 30$.

We will perform the same procedure for the kagome strip. However, for a controlled finite size scaling analysis, one encounters the problem that the system size cannot be chosen arbitrarily. The number of amenable system sizes for comparison is limited

(see section 3.3). A common divisor for the system sizes of 11 stars and 5 stars is 3. However, analysis for more than 11 stars cannot be conducted in the given time frame of this thesis. As explained earlier, the next useful system size for comparison consists of 17 stars and they should be treated in future analyses. This is because including them would be necessary to effectively find J_{crit} for $L \rightarrow \infty$. Nevertheless, the spin gap values and extrapolation for 5 and 11 stars are depicted in Figure 5.5.

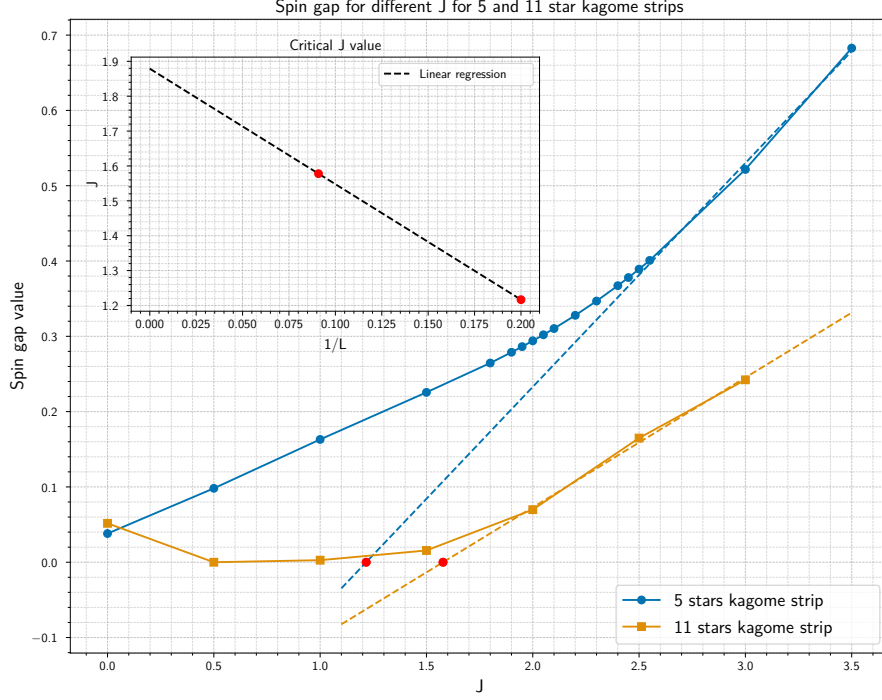


Figure 5.5: Spin gap value for 2 kagome strips of different sizes and for different values of J between $0.0 \leq J \leq 3.5$ for a filling of $n = 1/3$. The spin gap opening is approximated with a linear regression and then plotted over the inverse system size $1/L$ in the inset plot. The critical value is $J_{\text{crit}} = 1.88$ for $L = 5, 11$ and $J_{\text{crit}} = 1.89$ for $L = 36, 78$. The spin gap value for $J = 0.0$ for the 11 star kagome strip is neglected because of convergence issues. $\chi_{\text{max}} = 2000$, $n_{\text{sweeps}} = 30$.

The first thing that attracts attention is that the spin gap value for 11 stars at $J = 0.0$ is larger than the subsequent data points and the fact that for $J = 0.0$ the value is even finite at all. For $J = 0.0$ no spin interactions exist and consequently a spin-flip should not result in a shifted energy. The observations might be explained by finite-size effects, even though it is uncommon that the behavior is remedied immediately after increasing the system size by "only" 6 stars for all other data points. In fact, the first data point for 11 stars is not converged properly. Similar

to the plots for the densities in the previous chapter the local spin distribution can be visualized in the same manner for the state $S_z^{\text{tot}} = 1$. For $S_z^{\text{tot}} = 0$ we know that $\langle S_i^z \rangle = 0 \forall i$ due to the *Hohenberg-Mermin-Wagner theorem*. A green color indicates a positive value whereas red indicates a negative sign. The diameter of the drawn circles is again proportional to the absolute value. Figure 5.6 illustrates that the system does not converge, because the local spin distribution is not symmetric, and thus the plotted value for $J = 0.0$ is not the true spin gap Δ_S . Similar to the plots for the local density in Figures 5.2 and 5.3, the plots for the local observable S_i^z must show a symmetry if converged properly. More sweeps and a higher bond dimension might resolve this inconsistency. This inconsistency did also result in a negative value for Δ_S in another run, which contributes to the convergence problems. Similar to Figure 5.6 the plot for the 5 star strip for $J = 1.0$ also shows that the system did not properly converge although this value is not as large as the one depicted in Figure 5.6.

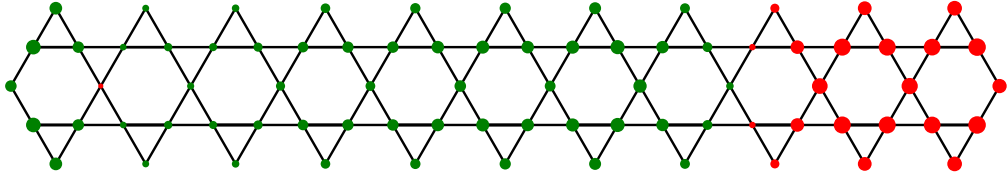


Figure 5.6: Local spin per site of a kagome strip consisting of 11 stars for $J = 0.0$ for $S_z^{\text{tot}} = 1$. Green indicates a positive value, whereas red indicates a negative sign. The spin value per lattice site is proportional to the diameter of the drawn circles. $\chi_{\text{max}} = 2000$, $n_{\text{sweeps}} = 30$.

Since we only have two data points, the extrapolation in Figure 5.5 can only be a preliminary attempt to analyze the data. As already explained, it would be necessary to also simulate systems consisting of 17, 23, \dots stars to ensure more reliability of J_{crit} . In both systems a kink at a certain J value can be identified which serves as a guide for creating the regression. The critical point is determined to be $J_{\text{crit}} = 1.88$. The spin-gap curve for the 11 star system appears more similar to the case of a chain and may be more reliable. Since there are only two data sets available, the critical value J_{crit} can vary depending on the visual interpretation and fitting approach used in the regression plots. If fewer data points are taken into account similar to Figure 5.4, the critical values can also be $J_{\text{crit}} = 1.61$, $J_{\text{crit}} = 1.48$ or $J_{\text{crit}} = 1.74$. Hence, J_{crit} is estimated to be $J_{\text{crit}} = 1.68 \pm 0.2$ by averaging over these values. This represents the midpoint between the largest and smallest value, with all determined

values lying within this error range. Despite the uncertainty, it seems that the critical value for the spin gap for the kagome system is actually smaller than for the chain. This statement can only be further justified and validated if data for more than two systems were available.

Apart from the fact that the spin plots can indicate that a system is not properly converged by symmetry arguments, they show an intriguing behavior. The spins form symmetrical local patterns. Figure 5.7 shows this for 11 stars and Figure 5.8 for 5 stars for $J = 0.5$, $J = 1.5$ and $J = 2.5$.

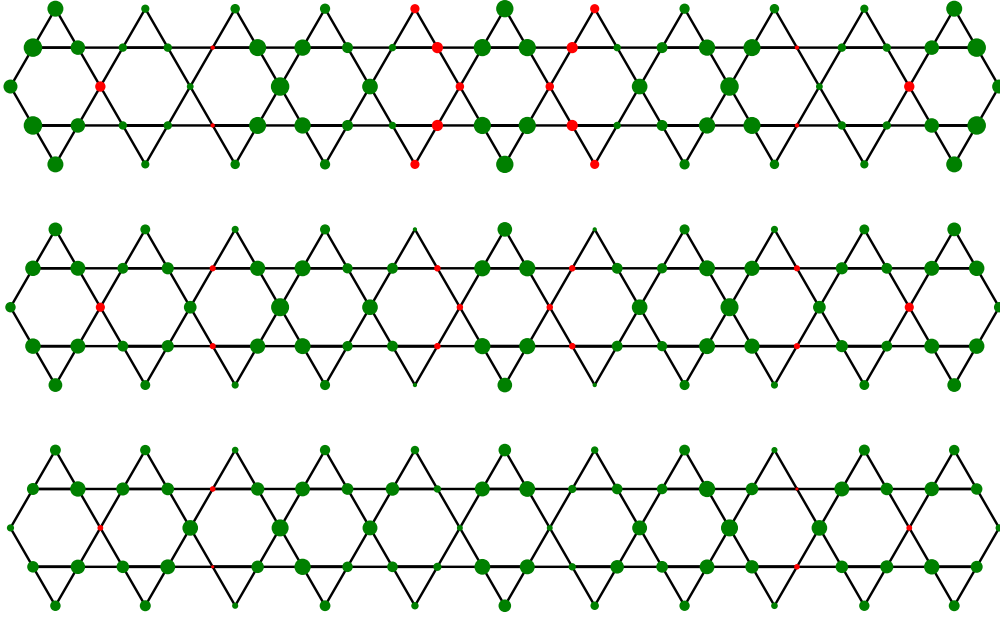


Figure 5.7: Local spin per site of a kagome strip consisting of 11 stars for $J = 0.0$ (top), $J = 0.5$ (middle) and $J = 2.5$ (bottom) for $S_z^{\text{tot}} = 1$. Green indicates a positive value, whereas red indicates a negative value. The spin value per lattice site is proportional to the diameter of the drawn circles. $\chi_{\text{max}} = 2000$, $n_{\text{sweeps}} = 30$.

For instance, the spin arrangement for the 5 star system at $J = 0.5$ shows a seemingly orderly but non-symmetrical configuration. The system probably did not converge for $J = 0.5$. The patterns raise various interesting questions. If simulations with more stars were possible, it would be interesting to investigate whether the patterns from Figure 5.7 repeat. While further quantitative analysis concerning these plots is beyond the scope of this thesis, future studies could be directed towards computing the total spin per star or entanglement measures.

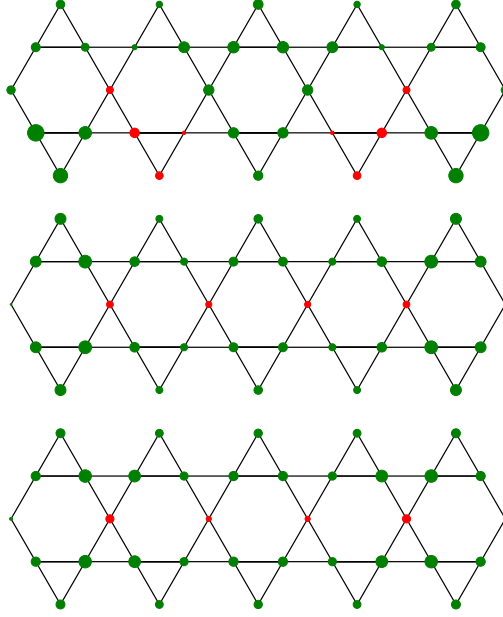


Figure 5.8: Local spin per site of a kagome strip consisting of 5 stars for $J = 0.0$ (top), $J = 0.5$ (middle) and $J = 2.5$ (bottom) for $S_z^{\text{tot}} = 1$. Green indicates a positive value, whereas red indicates a negative value. The spin value per lattice site is proportional to the diameter of the drawn circles. $\chi_{\text{max}} = 2000$, $n_{\text{sweeps}} = 30$.

5.3 Singlet Pairing Correlation Functions for QLRO

One way to detect a superconducting phase is to investigate the LRO, or in our case QLRO, in the system as explained in 2.2.2. To compute the singlet pairing correlation function $P = \langle \Delta_i^\dagger \Delta_j \rangle$ with the ground state vector $|\psi_0\rangle$, we use the definition for Δ_i as the pairing operator based on the bonds of the kagome strip as explained in section 3.3.3. With the definition of distance for the kagome strip, which is introduced in section 3.3.2, the entries of P_{ij} are plotted against the distance $|i - j|$. Since there are several configurations for realizing the same distance $|i - j|$, we average over all possible values. Additionally, we exclude 2 sites from the boundaries to reduce boundary effects. This procedure is more beneficial for the chain because more values for each distance $|i - j|$ exist than for the kagome strip. The analysis for the distances for 7 stars is equivalent to a chain with 14 sites (see 3.3.2) although 7 stars already consist of 50 sites. This procedure is also done for the density-density correlation function $N_{ij} = \langle \hat{n}_i \hat{n}_j \rangle - \langle \hat{n}_i \rangle \langle \hat{n}_j \rangle$ and the spin-spin correlation function $S_{ij} = \langle S_z^i S_z^j \rangle$. As explained in sections 2.2.2 and 2.2.3, the decay of the

correlation functions indicates the presence or absence of a superconducting phase. Theoretically, one must fit the decay of the correlation functions and analyze which correlation function decays the slowest. If the singlet pairing correlation function P_{ij} decays slowest, a superconducting phase is indicated. Here, due to the time constraints we forego this and look at the decay qualitatively.

For the chain with filling $n = 1/3$, it is noticeable that the singlet superconducting phase is present for $2.5 \leq J \leq 3.0$ (see phase diagram in Fig. 3.1). For smaller J values we expect other phases to dominate and thus other correlation functions than the singlet pairing correlation function $P_{ij} = \langle \Delta_i^\dagger \Delta_j \rangle$ to be dominant, i.e. they have a slower decay with distance $|i - j|$. A comparison with the spin-spin correlation function $S_{ij} = \langle S_z^i S_z^j \rangle$ and the density-density correlation function $N_{ij} = \langle n_i n_j \rangle - \langle n_i \rangle \langle n_j \rangle$ verifies this statement. Figures 5.9 and 5.10 show the decay of both of these correlation functions for a 78 site chain with filling $n = 1/3$ for the values $J = 0.0$, $J = 2.5$ and $J = 3.0$.

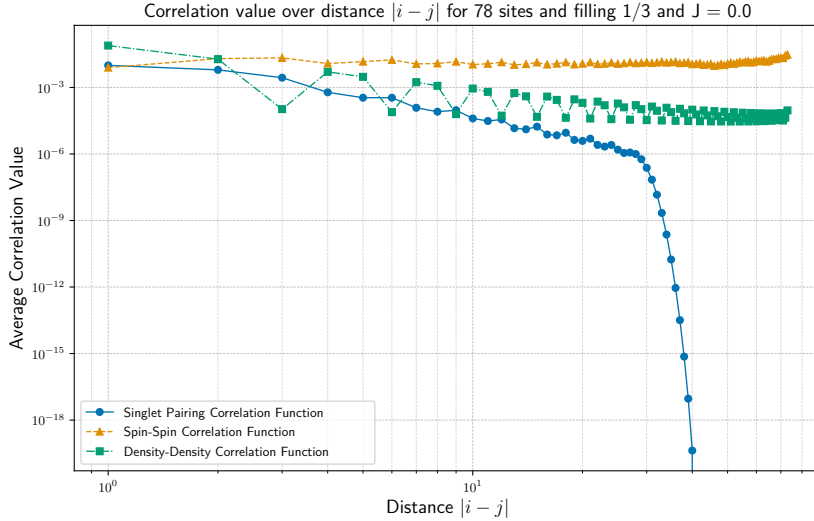


Figure 5.9: Correlation functions $\langle \Delta_i^\dagger \Delta_j \rangle$, $\langle S_z^i S_z^j \rangle$ and $\langle n_i n_j \rangle - \langle n_i \rangle \langle n_j \rangle$ over distance $|i - j|$ for $J = 0.0$ for a chain with 78 sites and filling $n = 1/3$. The singlet pairing correlation function decays the fastest indicating the absence of a superconducting phase for $J = 0.0$ as expected from [MMM11]. $\chi_{\max} = 2000$, $n_{\text{sweeps}} = 30$.

For $J = 0.0$ the dominant correlation function is the spin-spin correlation function and not the singlet pairing correlation function. This was anticipated because the superconducting phase is expected for $J \geq 2.5$ according to [MMM11]. Hence, for

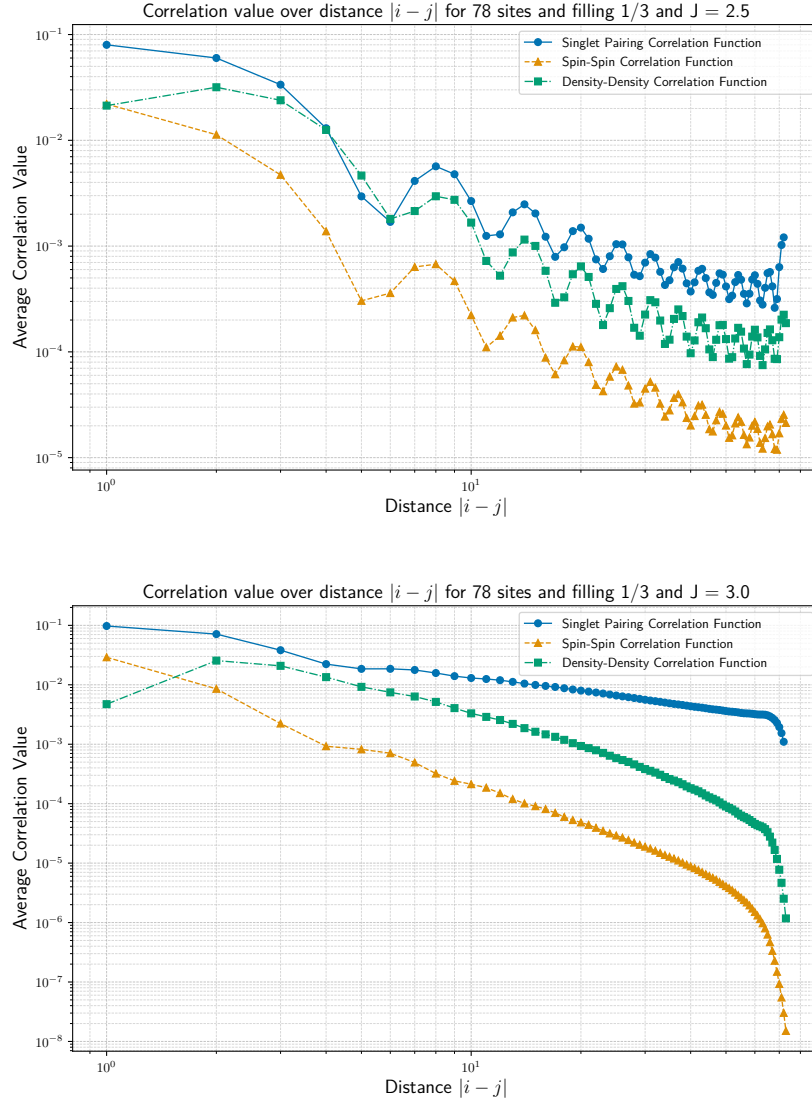


Figure 5.10: Correlation functions $\langle \Delta_i^\dagger \Delta_j \rangle$, $\langle S_z^i S_z^j \rangle$ and $\langle n_i n_j \rangle - \langle n_i \rangle \langle n_j \rangle$ over distance $|i - j|$ for $J = 2.5$ (top) and $J = 3.0$ (bottom) for a chain with 78 sites and filling $n = 1/3$. The decay indicates the start of a superconducting phase around $2.5 \leq J \leq 3.0$. $\chi_{\max} = 2000$, $n_{\text{sweeps}} = 30$.

$J = 3.0$, the tendency of QLRO can be observed since the decay of P_{ij} is slower than that of the spin-spin and density-density correlation functions.

The fact that the correlation functions change the decay-behavior suggests that there must exist a point where the phase transition (or a crossover) happens. The behavior for $J = 1.5$ and $J = 2.0$ is depicted in 5.11. The correlation functions seem

5.3 Singlet Pairing Correlation Functions for QLRO

to intersect which indicates the phase transition should occur at around $J = 2$ in the thermodynamic limit.

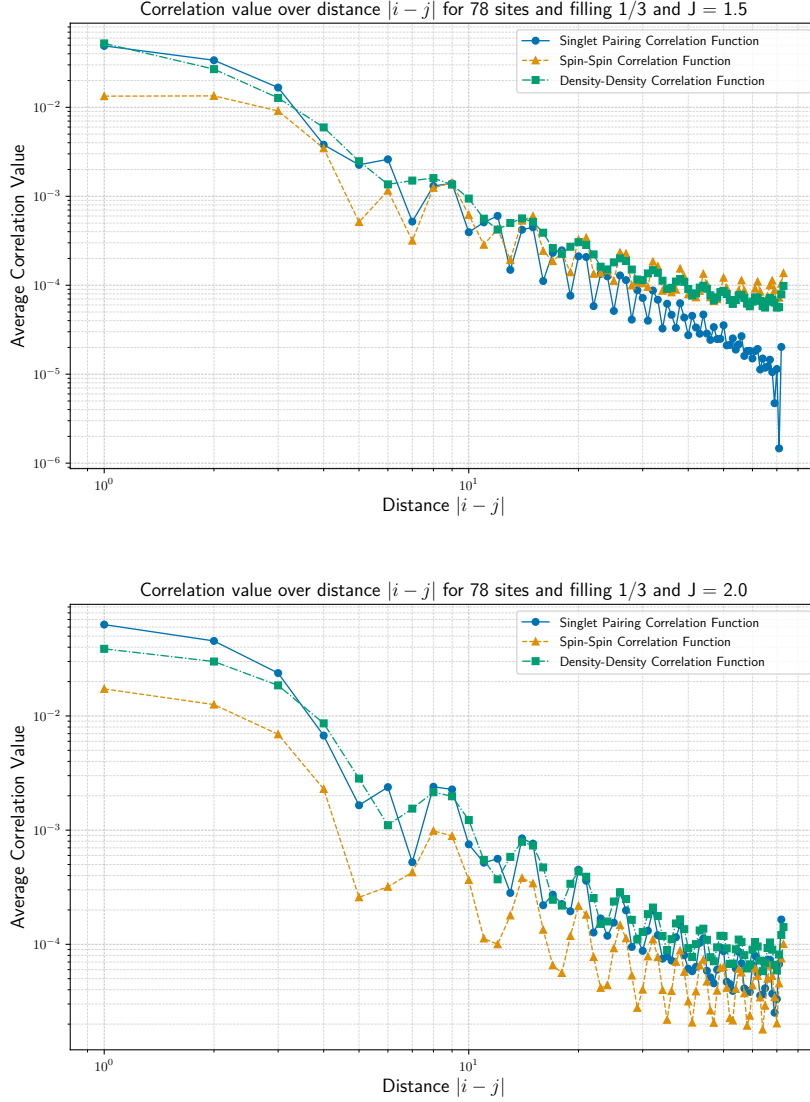


Figure 5.11: Correlation functions $\langle \Delta_i^\dagger \Delta_j \rangle$, $\langle S_z^i S_z^j \rangle$ and $\langle n_i n_j \rangle - \langle n_i \rangle \langle n_j \rangle$ over distance $|i - j|$ for $J = 1.5$ (top) and $J = 2.0$ (bottom) for a chain with 78 sites and filling $n = 1/3$. The correlation functions show an almost identical course indicating a change in phases to the superconducting phase for $J = 3.0$. $\chi_{\max} = 2000$, $n_{\text{sweeps}} = 30$.

Although there are fewer values to average over for 36 sites, identical tendencies can be observed for this chain geometry. Due to time considerations it is not possible to compute the complete singlet pairing correlation function for 11 stars and a filling of

$n = 1/3$ as can be seen in the next chapter. This is required to find the eigenvalues of P_{ij} (see section 2.2.2). For the decay analysis not every entry P_{ij} is required since we are only interested in the bonds and sites of the upper chain (see 3.3.2). Thus the number of bonds needed to be considered decreases from 130 to 21 and the number of computations reduces to only 2.61% of the originally required expectation values $\langle \psi_0 | \Delta_i^\dagger \Delta_j | \psi_0 \rangle$ for all entries P_{ij} . The results are depicted in Figures 5.12 and 5.13.

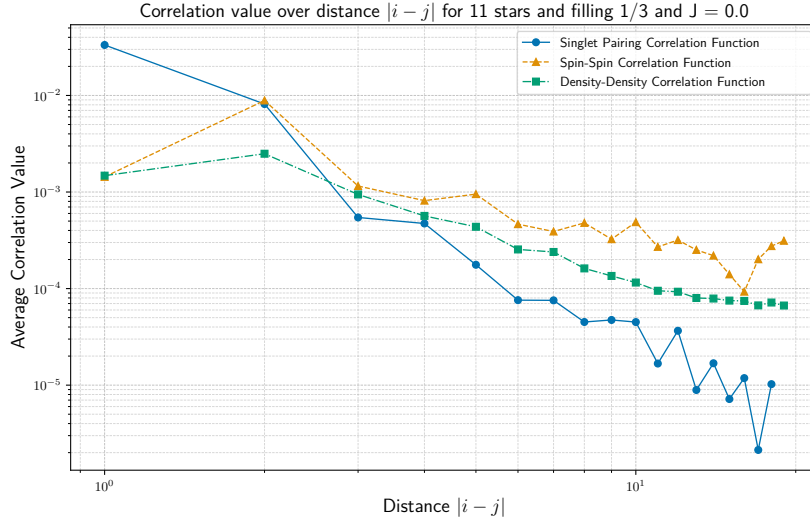


Figure 5.12: Correlation functions $\langle \Delta_i^\dagger \Delta_j \rangle$, $\langle S_z^i S_z^j \rangle$ and $\langle n_i n_j \rangle - \langle n_i \rangle \langle n_j \rangle$ over distance $|i-j|$ for $J = 0.0$ for a 11 star kagome strip and filling $n = 1/3$. $\chi_{\max} = 2000$, $n_{\text{sweeps}} = 30$.

Again, it is qualitatively illustrated in Figure 5.12 that the singlet pairing correlation function is not dominant for $J = 0$. Moreover, Figure 5.13 shows that for $J = 3.0$ the singlet pairing correlation function does not decay as slowly as it did for the chain. It is possible to argue that the superconducting phase might be realized for $J = 3.0$. The next step involves fitting the correlation function and comparing the decay exponents. This comparison is crucial for further analysis. Another aspect is that the superconducting phase might not occur around $2.5 \leq J \leq 3.0$ for the kagome strip in contrast to the chain. Therefore, P_{ij} is also computed for $J = 3.5$ and depicted in Figure 5.13.

5.3 Singlet Pairing Correlation Functions for QLRO

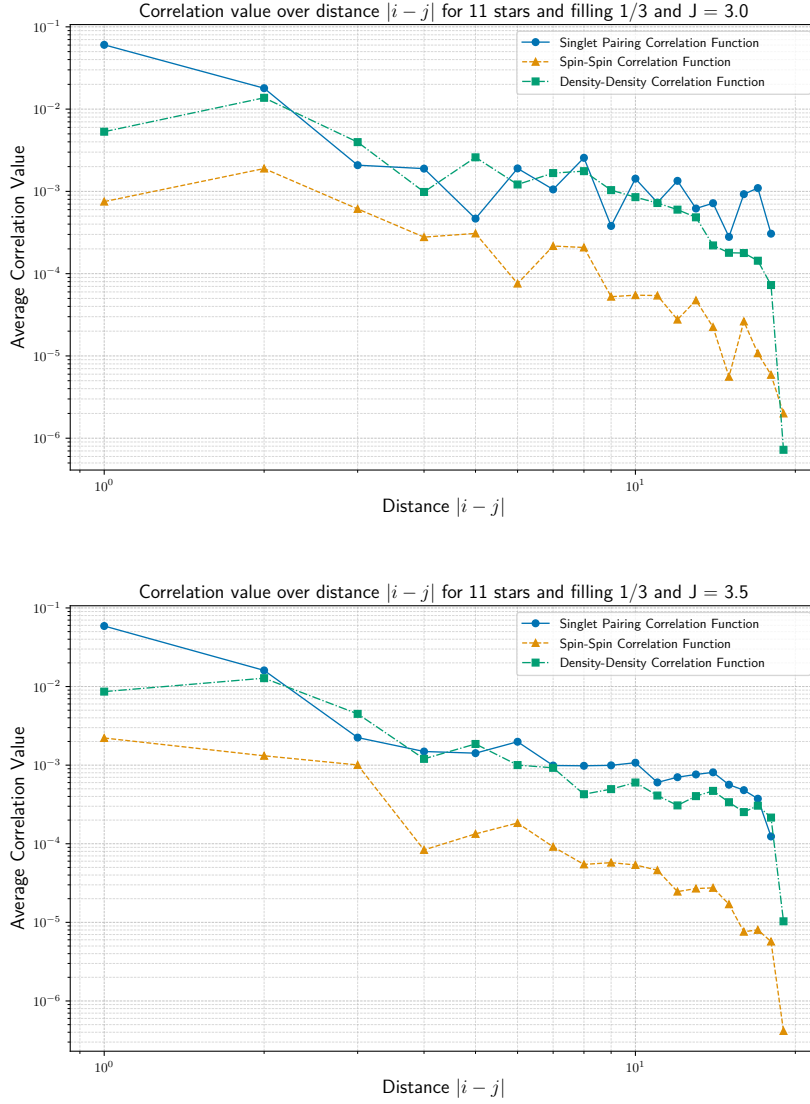


Figure 5.13: Correlation functions $\langle \Delta_i^\dagger \Delta_j \rangle$, $\langle S_z^i S_z^j \rangle$ and $\langle n_i n_j \rangle - \langle n_i \rangle \langle n_j \rangle$ over distance $|i-j|$ for $J = 3.0$ (top) and $J = 3.5$ (bottom) for a 11 star kagome strip and filling $n = 1/3$. $\chi_{\max} = 2000$, $n_{\text{sweeps}} = 30$.

It is arguable for which J value the superconducting phase emerges, however, the data suggests a small shift towards the larger values of J compared to the chain. Instead of a range between $J = 2.5$ and $J = 3.0$, a J value around $3.0 \leq J \leq 3.5$ seems more reasonable. Due to the fact that we cannot compute all entries of the singlet pairing correlation matrix for 11 stars and a filling of $n = 1/3$, 9 stars for a filling of $n = 1/8$ were also simulated. The case for 9 stars is illustrated in the appendix in section 7.3 in Figures 7.5 and 7.6. Figure 7.6 suggests again that the

superconducting phase might be shifted towards slightly larger J values, though not as much as for the higher filling of $n = 1/3$. The superconducting phase might be around $J = 3 \pm 0.25$ for filling $n = 1/8$ compared to $J = 3.25 \pm 0.25$ for filling $n = 1/3$ for the kagome strips. To support the statement that the superconducting phase is shifted towards larger J for the kagome strip, more data is required, preferably from larger systems.

5.4 Eigenvalue Analysis for QLRO

Another indication for quasi-long-range order is the behavior of the eigenvalues of P_{ij} . A dominant eigenvalue λ_{\max} of the singlet pairing correlation function $\langle \Delta_i^\dagger \Delta_j \rangle$ indicates LRO/ QLRO in the system and thus a superconducting phase. P_{ij} is of the dimension of the number of bonds in the system which is around the magnitude of 100. The matrix is diagonalized numerically using the `eigen()` function provided by the `LinearAlgebra` standard library module.

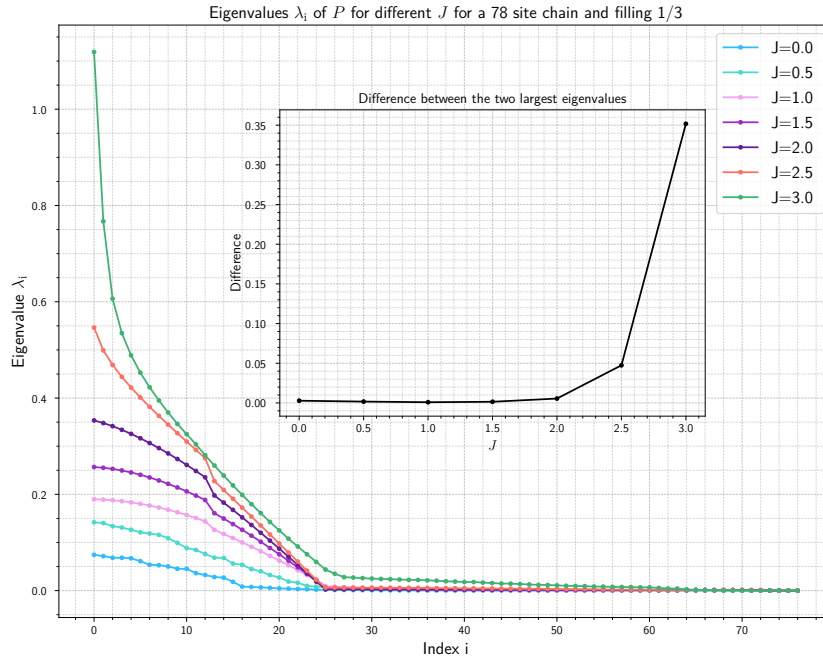


Figure 5.14: Eigenvalues of the singlet pairing correlation function $\langle \Delta_i^\dagger \Delta_j \rangle$ for a chain consisting of 78 sites for a filling of $n = 1/3$ for different J values. The difference between the two largest eigenvalues is substantially larger for $J = 3.0$ compared to $J = 0.0$. The dominance of one eigenvalue becomes apparent starting at $J \approx 2.0$. $\chi_{\max} = 2000$, $n_{\text{sweeps}} = 30$.

For a chain, it is known from [MMM11] that the singlet superconducting phase starts around $J = 2.5$ for a filling of $n = 1/3$. For a chain consisting of 78 sites and a filling of $n = 1/3$, the singlet pairing correlation function is computed, diagonalized and the eigenvalues for different J are depicted in Figure 5.14. The eigenvalues decay faster when increasing J and this behavior is more evident when plotting the difference between the two largest eigenvalues in the inset plot of 5.14, which provides more insights into the extent λ_{\max} can be designated dominant. The difference starts noticeably around $J = 2.0$, but the jump from $J = 2.5$ to $J = 3.0$ stands out. This supports the statements from the previous section and findings of [MMM11] depicted in the phase diagram 3.1.

Data for the kagome strip for 11 stars and filling $n = 1/3$ was not simulated because the computations exceed the time frame of this work. Therefore, Figure 5.15 depicts the eigenvalues and the difference of the two largest eigenvalues of the singlet pairing correlation function for a 64 site chain and a filling of $n = 1/8$ (lower fillings facilitate the convergence) to compare with the kagome strip.

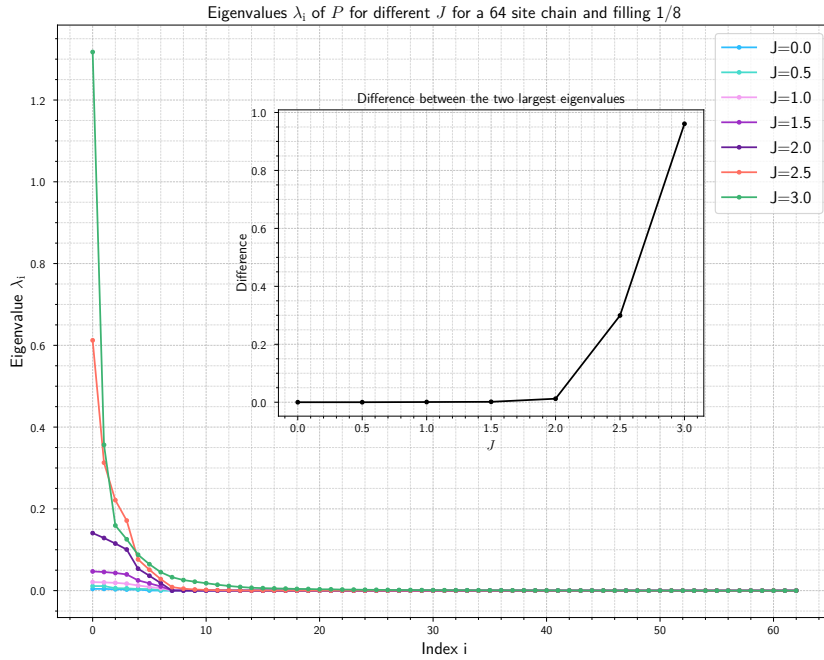


Figure 5.15: Eigenvalues of the singlet pairing correlation function $\langle \Delta_i^\dagger \Delta_j \rangle$ for a chain consisting of 64 sites for a filling of $n = 1/8$ for different J values. The difference between the two largest eigenvalues is increased for $J \geq 3.0$ compared to $J = 0.0$. The dominance of one eigenvalue becomes apparent starting at $J \approx 2.0$. $\chi_{\max} = 2000$, $n_{\text{sweeps}} = 30$.

Although Figure 5.14 and 5.15 do not depict chains of the same size, we can see that for filling $n = 1/8$ the difference between the two largest eigenvalues becomes apparent earlier than for $n = 1/3$. This complies with the phase diagram for the chain in Fig. 3.1 because the SG+SS curve tilts to the top right when increasing n . For lower fillings the emergence of the superconducting phase is expected to be earlier. Regardless, Figure 5.15 should serve as a comparison for the kagome strip consisting of 9 stars with filling $n = 1/8$ depicted in Figure 5.16.

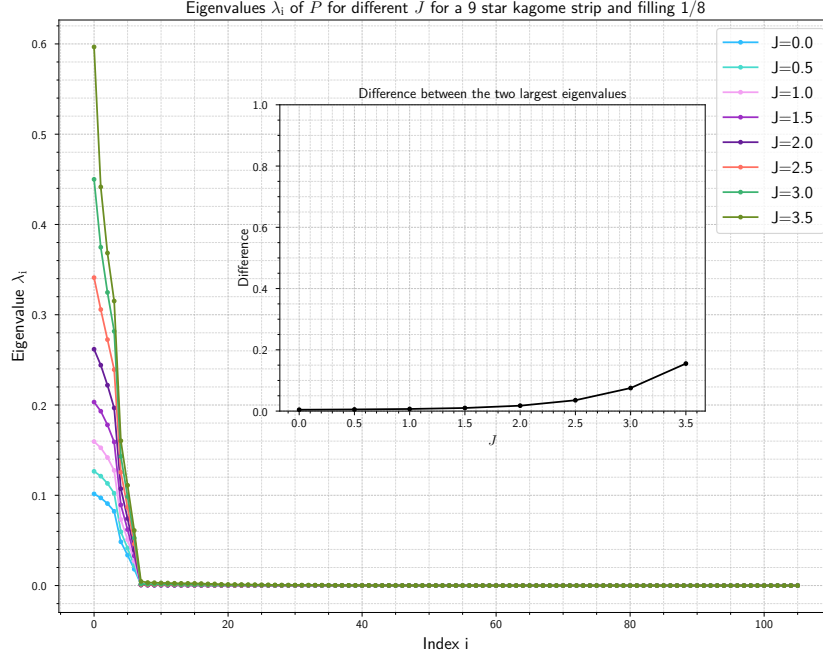


Figure 5.16: Eigenvalues of the singlet pairing correlation function $\langle \Delta_i^\dagger \Delta_j \rangle$ for a 9 star kagome strip for a filling of $n = 1/8$ for different J values. The difference between the two largest eigenvalues is increased for $J = 3.5$ compared to $J = 0.0$. The y -axis of the inset plot is scaled identically to Fig. 5.15 for better comparison. The eigenvalue differences are not as large as for the chain. $\chi_{\max} = 2000$, $n_{\text{sweeps}} = 30$.

The eigenvalue difference in Figure 5.16 tends to get larger for larger J . However, in contrast to the chain, the absolute value of the difference is lower. The peak is not as large as in Figure 5.15. Since there did not exist a significant peak between $J = 2.5$ and $J = 3.0$, the system was simulated for $J = 3.5$ as well. Although the peak is not even comparable to the chain for $J = 3.5$, it again seems as if the superconducting phase is shifted towards the right. This cannot be answered definitively. However, illustrating both of the eigenvalue differences in one plot in Figure 5.17 excludes the

interpretation that the superconducting phase opens significantly earlier. On the whole, both lines behave similarly, except for the fact that the differences for the kagome strip are smaller.

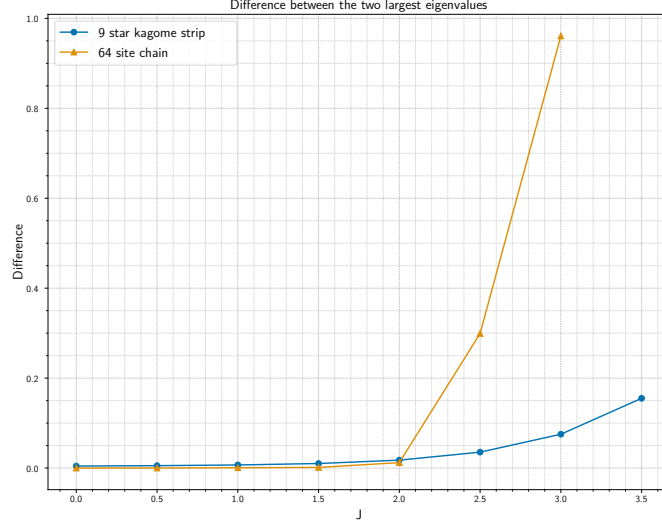


Figure 5.17: Difference between the two largest eigenvalues for a 64 site chain and a 9 star kagome strip for a filling of $n = 1/8$. The plot for the chain shows two highly visible kinks whereas the line for the kagome strip rises smoothly. $\chi_{\max} = 2000$, $n_{\text{sweeps}} = 30$.

Figure 5.17 clearly shows a difference between the two largest eigenvalues of the chain and the kagome strip. It is not clear whether the smoothness at larger J can be traced back to finite size effects. Larger systems would need to be simulated to compare this behavior.

5.5 Sketch of the Phase Diagram for Two Different Fillings

In this section, we summarize the previous results for the ground state phase diagram of the t - J model on kagome strips. However, it is understood from previous discussions that these are rough sketches and more data is needed to be able to draw the phase diagrams with greater accuracy. Despite this, the sketches for a filling of $n = 1/3$ (Fig. 5.18) and $n = 1/8$ (Fig. 5.19) summarize the results and the associated analysis from the previous sections. For the chain and a filling of $n = 1/3$

we found that the spin gap opens at $J_{\text{crit}} = 2.25$ and can support the findings of [MMM11] of a superconducting phase at around $2.5 \leq J \leq 3.0$.

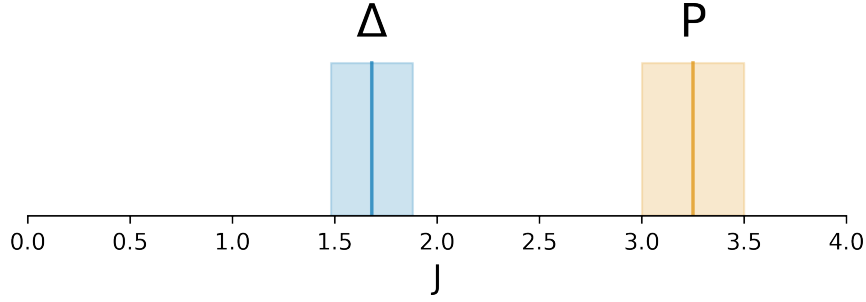


Figure 5.18: Sketch of the ground state phase diagram of the t - J model on kagome strips for a filling of $n = 1/3$. The spin gap opens at $J_{\text{crit}} = 1.68 \pm 0.2$ (Δ) and the superconducting phase is evident for $J = 3.25 \pm 0.5$ according to the singlet pairing correlation functions $P_{ij} = \langle \Delta_i^\dagger \Delta_j \rangle$ (P).

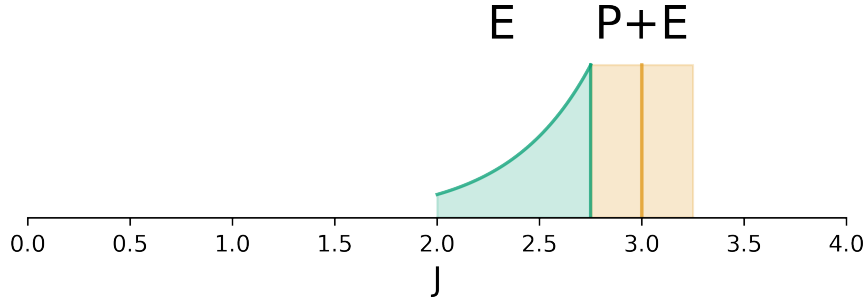


Figure 5.19: Sketch of the ground state phase diagram of the t - J model on kagome strips for a filling of $n = 1/8$. The superconducting phase is evident for $J = 3.0 \pm 0.25$ according to the singlet pairing correlation functions $P_{ij} = \langle \Delta_i^\dagger \Delta_j \rangle$ (P) and the eigenvalues of P_{ij} (E). The eigenvalue analysis raises the question if the superconducting phase might open earlier, possibly around $J = 2.0$ (E). The green curve indicates the slow growth of the eigenvalues for the kagome strip compared to the chain. There is no spin gap shown, because only one system size is available.

The sketch in Figure 5.18 shows a spin gap opening at 1.68 ± 0.2 according to the analysis of Figure 5.5 in section 5.2. In section 5.3 the superconducting phase is determined to emerge for a larger J than for the chain. However, section 5.4 also raises the question whether the superconducting phase might open earlier than $J = 2.75$ for $n = 1/8$ (like the chain), which is indicated by the green exponential decay from $J = 2.75$ towards smaller J in Figure 5.19.

Figure 5.18 also shows that the spin gap opens before the superconducting phase emerges for the kagome strips. In contrast to the chain, this can happen as shown

5.5 Sketch of the Phase Diagram for Two Different Fillings

in ref. [BOKM23] for the two-leg t - J ladder at low fillings or for generalized t - J models in ref. [MMGH17].

Due to the lack of data it is not reasonable to show the spin gap for the 9 star system with filling $n = 1/8$. Therefore, Figure 5.19 does not depict the critical J_{crit} value for which the spin gap opens. In general, the figures show that the phases move towards smaller J values for smaller fillings. This is similar to the results for the chain 3.1. Thus, at low fillings the start of the superconducting phase would probably also show a tilt to the top direction. However, this requires further investigation and is a task for future studies.

6 Summary and Outlook

In this thesis, different phases of the t - J model on kagome strips were investigated. The first challenge we had to address was the convergence of the DMRG algorithm for the ground state energy E_0 and state vector $|\psi_0\rangle$ on the kagome strip. Since DMRG is a variational method, convergence to the true ground state cannot be guaranteed, however the implementation of a noise term increased the likelihood that one can assume that the results are generally relatively reliable. The convergence is worse in systems with a larger filling n and larger system sizes. To ensure that the computed energies and state vectors are meaningful, local observables were visualized to ensure symmetries. The emergence of symmetric patterns in the local density and later also in the local spin distribution on the kagome strip suggest a good convergence. The exact opposite reveals problematic cases such as the treatment of $J = 0.0$. Generally speaking, the ground state computation can use more sweeps and a larger bond dimension to ensure better accuracy.

After obtaining reasonable results for E_0 , the spin gap value was computed. Therefore, for one filling n the critical J_{crit} for which the spin gap opens is plotted over the inverse system size L . An extrapolation then yields the critical value in the thermodynamic limit. In contrast to the chain, which was simulated for several system sizes, there exist only two lattice sizes for the kagome strips, which could be treated within the time constraints of this thesis. Due to the difficulties in finding common divisors for the number of sites in the kagome strip, there are limited options to simulate. Here, only 5 and 11 stars for a filling of $n = 1/3$ were simulated. This leads to a relatively large uncertainty of the spin gap value for the kagome strips compared to the chains. The results for the chain can be compared to those from ref. [MMM11]. The results for the kagome strip suggest a shift of the point, at which the spin gap opens, towards smaller J values. Here, we specifically found $J = 1.68 \pm 0.2$. As already explained, future study must also consider at least the system consisting of 17 stars, since a regression through two points is not mean-

ingful. Additionally, more fillings than $n = 1/3$ need to be simulated in order to investigate if the J_{crit} tilts to the left/right for larger fillings n . This statement can be made about the superconducting phase, but unfortunately not about the spin gap as can be seen in the sketches of the phase diagrams in the Figures 5.18 and 5.19.

After analyzing the spin gap of the kagome strips, the entries of the correlation functions P_{ij} , S_{ij} and N_{ij} were plotted against the distance $|i - j|$ and their decay was evaluated. The dominance of the singlet pairing correlation function P_{ij} , indicated by a smaller decay than the other correlation functions, indicates quasi-long-range order and thus a potential superconducting phase. For the chain, the superconducting phase is around $2.5 \leq J \leq 3.0$, according to ref. [MMM11]. The superconducting phase for the kagome strips, however, suggest a shift towards larger J values. The superconducting phase is determined to start around $3.0 \leq J \leq 3.5$ for a filling of $n = 1/3$ and $2.75 \leq J \leq 3.25$ for a filling of $n = 1/8$. The curvature to the top right of the emergence of the superconducting phase for small fillings can also be observed for the chain in Fig. 3.1.

Another indication for quasi-long-range order is given by the eigenvalue analysis of the singlet pairing correlation function P_{ij} . The findings for the chain coincide with the findings from the previous section where the decay of the correlation functions was observed. For low fillings a curvature of the emergence of the superconducting phase is to be expected as also depicted in the phase diagram for the chain in Fig. 3.1. For the kagome strips for filling $n = 1/8$, however, we cannot give a definitive statement. On the one hand, the findings of the previous section of a superconducting phase at larger J values can be confirmed, but on the other hand the eigenvalues give rise to another interpretation. For the kagome strips with filling $n = 1/8$, the eigenvalue difference behaves similarly to the ones of the chain. Thus, the superconducting phase might start earlier than the stated interval of $2.75 \leq J \leq 3.25$ as indicated by the exponential decay in phase diagram 5.19, which is between 2.0 and 2.75.

This thesis raises many questions, but we fundamentally understand how to proceed. One of the main aspects is connected to all technical aspects to handle the convergence problems. Although a more sensible numbering of the sites of the kagome strip than the one introduced in section 3.3.1 may exist, future studies could rather focus on implementing a proper warm-up procedure for the initial state guess for the

DMRG algorithm. One should also use more sweeps and possibly a larger bond dimension χ_{\max} to obtain more accurate results. This is especially unavoidable when treating larger systems sizes like 17 stars, which are required to obtain sensible results for the spin gap as explained in section 5.2.

It is unclear why the superconducting phase should shift towards larger J values. Therefore, the question arises whether the particular phase is actually a superconducting phase. A possible interpretation is that we encountered phase separation at these high J values, just like for the chain with $J = 3.5$ and $n = 1/3$ as depicted in the phase diagram in Figure 3.1. However, we did not encounter increased convergence problems for these larger J values as it would be expected for this phase, so that probably SC is obtained.

In this thesis, the t - J model with Hamiltonian of Eq. 3.1 was implemented. There exist several other generalized t - J -like models, which could be interesting to investigate on the kagome strips. Reference [MMGH17] shows that a generalized t - J model results in a richer phase diagram for the chain. For the Kagome strip, we cannot make any definitive statements about this behavior. However, the kagome strips seem to be comparable to the chain and thus it would be interesting to further investigate this.

7 Appendix

7.1 Implementations

In this section the important code implementations, which were used to simulate the results from chapter 5 are given here.

```
1 sites = siteinds("tJ", N; conserve_qns=true)
2 ampo = AutoMPO()
3
4 for j in 1:N
5     for neighbor in neighbors[j]
6         if neighbor > j
7             # Hopping term
8             add!(ampo, -t, "Cdagup", j, "Cup", neighbor)
9             add!(ampo, -t, "Cdagup", neighbor, "Cup", j)
10            add!(ampo, -t, "Cdagdn", j, "Cdn", neighbor)
11            add!(ampo, -t, "Cdagdn", neighbor, "Cdn", j)
12
13            # Spin interaction term
14            add!(ampo, 0.5 * J, "S+", j, "S-", neighbor)
15            add!(ampo, 0.5 * J, "S-", j, "S+", neighbor)
16            add!(ampo, J, "Sz", j, "Sz", neighbor)
17
18            add!(ampo, -0.25 * J, "Ntot", j, "Ntot",
19                  neighbor)
20        end
21    end
22 end
23 H = MPO(ampo, sites)
```

Figure 7.1: Implementation of the t - J model Hamiltonian 3.1.

```

1 function precompute_ops(bonds, sites, len)
2     half = 0.5
3     minus_half = -0.5
4     results = Dict{Tuple{Int, Int}, Any}()
5     for k in 1:len
6         for l in 1:len
7
8             os = OpSum()
9             i_1 = bonds[k][1]
10            i_2 = bonds[k][2]
11            j_1 = bonds[l][1]
12            j_2 = bonds[l][2]
13
14            os .+= (half, "Cdagdn", i_1, "Cdagup", i_2, "
15                    Cup", j_2, "Cdn", j_1)
16            os .+= (minus_half, "Cdagdn", i_1, "Cdagup",
17                    i_2, "Cdn", j_2, "Cup", j_1)
18            os .+= (minus_half, "Cdagup", i_1, "Cdagdn",
19                    i_2, "Cup", j_2, "Cdn", j_1)
20            os .+= (half, "Cdagup", i_1, "Cdagdn", i_2, "
21                    Cdn", j_2, "Cup", j_1)
22
23            results[(k, l)] = MPO(os, sites)
24        end
25    end
26    return results
27 end
28
29 function compute_expectation_value(delta_sum, psi)
30     return inner(psi', delta_sum, psi)
31 end
32
33 for k in 1:len
34     delta_sums = [precomputed_ops[(k, l)] for l in 1:len]
35     expectation_values = map(delta_sum ->
36         compute_expectation_value(delta_sum, psi),
37         delta_sums)
38     println("iteration $k of $len")
39     pairing_corr_matrix[k, :] = expectation_values
40 end

```

Figure 7.2: Implementation of the singlet pairing correlation function $P_{ij} = \langle \Delta_i^\dagger \Delta_j \rangle$.

```

1 H = MPO(ampo, sites)
2 psi0 = randomMPS(sites, initial_state)
3 nsweeps = 30
4 maxdim = [10, 20, 40, 75, 100, 150, 200, 250, 300, 350,
           400, 500, 600, 700, 800, 900, 1000, 1100, 1200, 1300,
           1400, 1500, 1600, 1700, 1800, 1900, 2000]
5 cutoff = [1E-12]
6 noise = [1E-8, 0.0]
7 energy,psi = dmrg(H,psi0; nsweeps, maxdim, cutoff, noise)

```

Figure 7.3: Implementation of the DMRG algorithm with a noise term. H is defined in Figure 7.1.

```

1 function create_random_initial_state(filled_spots, N)
2     initial_state = ["Emp" for n in 1:N]
3     if filled_spots > 0
4         positions = randperm(N)[1:filled_spots]
5         for i in 1:filled_spots
6             if isodd(i)
7                 initial_state[positions[i]] = "Up"
8             else
9                 initial_state[positions[i]] = "Dn"
10            end
11        end
12    end
13    return initial_state
14 end

```

Figure 7.4: Implementation of the random initial state definition, which is required for initializing a MPS.

7.2 Lanczos Algorithm

The utilization of algorithms can be an effective way to approximate the ground state and vectors for large system sizes L . The Lanczos Algorithm [Lan50] is a frequently used option for these problems. Often we are only interested in the ground state of the system. Therefore, the Lanczos Algorithm can be used, providing a fast way to approximate the ground state energy of H as this method ensures that only a significantly smaller matrix needs to be diagonalized. The Algorithm works as follows [Man22, cf. p. 212]:

Initialization:

Choose a random vector $|u_0\rangle$ (in practice, one can often use a vector where each entry is 1).

First step of the iteration rule:

$$|u_1\rangle = H|u_0\rangle - \frac{\langle u_0|H|u_0\rangle}{\langle u_0|u_0\rangle}|u_0\rangle.$$

Further iteration steps $n > 1$:

$$|u_{n+1}\rangle = H|u_n\rangle - \underbrace{\frac{\langle u_n|H|u_n\rangle}{\langle u_n|u_n\rangle}}_{=:a_n}|u_n\rangle - \underbrace{\frac{\langle u_n|u_n\rangle}{\langle u_{n-1}|u_{n-1}\rangle}}_{=:b_n^2}|u_{n-1}\rangle.$$

The order- k Krylov subspace is given by $\text{span}\{|u\rangle, H|u\rangle, \dots, H^{k-1}|u\rangle\}$. The Hamiltonian H is projected into the Krylov subspace and is represented by a tridiagonal matrix T_k [Man22, p.211-213]

$$T_k = \begin{pmatrix} a_0 & b_1 & 0 & \cdots & 0 \\ b_1 & a_1 & b_3 & & \vdots \\ 0 & b_3 & \ddots & \ddots & 0 \\ \vdots & & \ddots & a_{k-1} & b_k \\ 0 & \cdots & 0 & b_k & a_k \end{pmatrix}.$$

The number k corresponds to the count of iterations executed in the Lanczos algorithm. Typically, k is significantly smaller than the dimension of the complete Hamiltonian (less than 100), which allows this matrix H_k to be diagonalized faster. Additionally, T_k can be diagonalized faster because it is tridiagonal [BBF16]. Let $|v\rangle = \sum_{i=1}^k v_i \hat{e}_i$ be the ground state eigenvector of the reduced Hamiltonian \hat{H}_k , then the ground state of H can be approximated with $|\psi_0\rangle = \sum_{i=1}^k v_i |\psi_i\rangle$.

7.3 Correlation Functions for 9 Stars

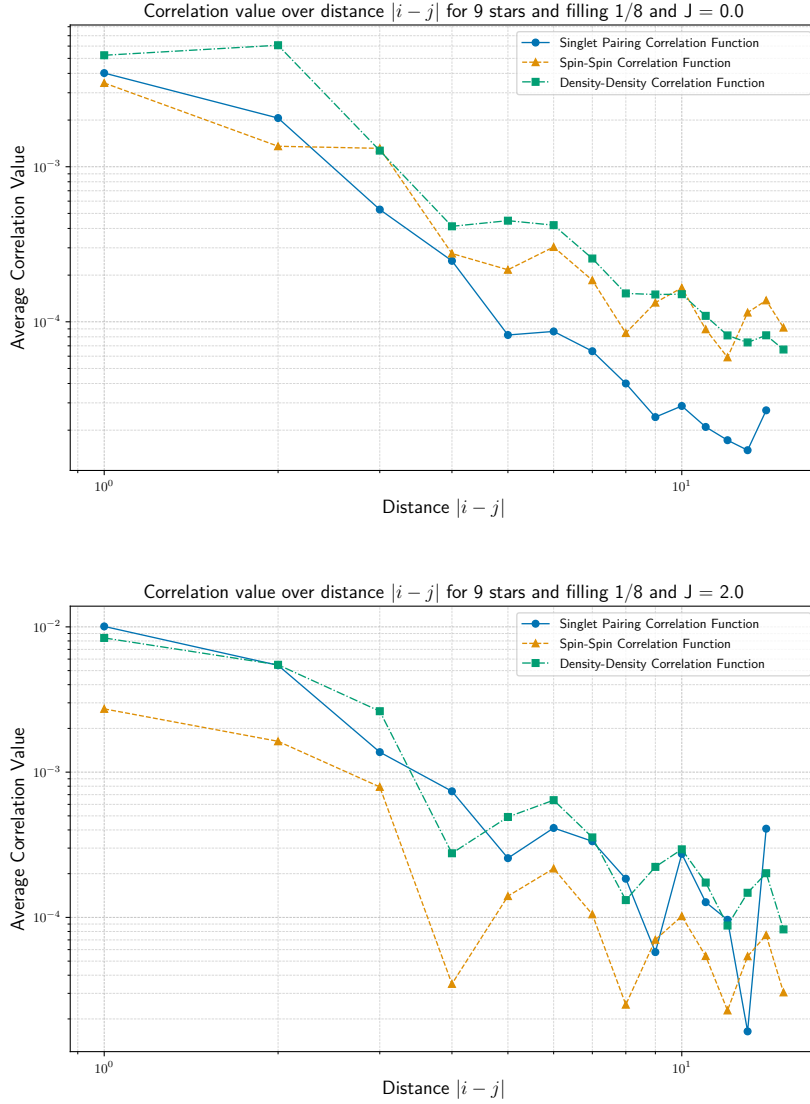


Figure 7.5: Correlation functions $\langle \Delta_i^\dagger \Delta_j \rangle$, $\langle S_z^i S_z^j \rangle$ and $\langle n_i n_j \rangle - \langle n_i \rangle \langle n_j \rangle$ over distance $|i - j|$ for $J = 0.0$ (top) and $J = 2.0$ (bottom) for a 9 star kagome strip and filling $n = 1/8$. The correlation functions show an almost identical course indicating a change a phases to the superconducting phase for $J = 3.0$. $\chi_{\max} = 2000$, $n_{\text{sweeps}} = 30$.

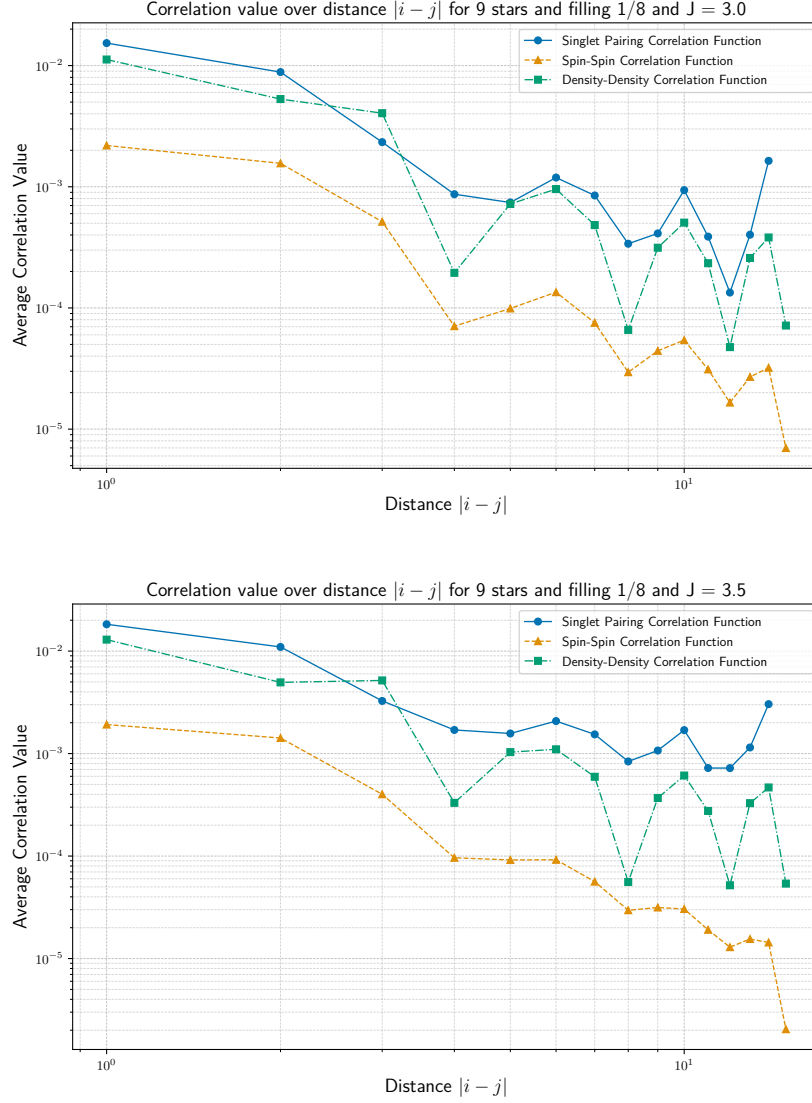


Figure 7.6: Correlation functions $\langle \Delta_i^\dagger \Delta_j \rangle$, $\langle S_z^i S_z^j \rangle$ and $\langle n_i n_j \rangle - \langle n_i \rangle \langle n_j \rangle$ over distance $|i-j|$ for $J = 3.0$ (top) and $J = 3.5$ (bottom) for a 9 star kagome strip and filling $n = 1/8$. The correlation functions show an almost identical course indicating a change a phases to the superconducting phase for $J = 3.0$. $\chi_{\max} = 2000$, $n_{\text{sweeps}} = 30$.

Bibliography

- [ABCF17] Rafael Andrade, Tibérius Bonates, Manoel Campêlo, and Mardson Ferreira. Minimum linear arrangements. *Electronic Notes in Discrete Mathematics*, 62:63–68, 2017. LAGOS’17 – IX Latin and American Algorithms, Graphs and Optimization.
- [And87] P. W. Anderson. The resonating valence bond state in la_2cuo_4 and superconductivity. *Science*, 235(4793):1196–1198, 1987.
- [And05] Natan Andrei. *beautiful models: 70 years of exactly solved quantum many-body problems*. *Phys. Today*, 58(9):58–60, September 2005.
- [Aue94] Assa Auerbach. *Interacting Electrons and Quantum Magnetism*. Springer-Verlag, 1994.
- [BBF16] Annette Burden, Richard Burden, and J. Faires. *Numerical Analysis, 10th ed.* 01 2016.
- [BK18] Amandeep Singh Bhatia and Ajay Kumar. Quantifying matrix product state. *Quantum Inf. Process.*, 17(3), March 2018.
- [BM86] J. G. Bednorz and K. A. Müller. Possible high- T_c superconductivity in the ba_2cuo_3 system. *Zeitschrift für Physik B Condensed Matter*, 64(2):189–193, Jun 1986.
- [BOKM23] Steffen Bollmann, Alexander Osterkorn, Elio J. König, and Salvatore R. Manmana. Lifshitz transition in the phase diagram of two-leg t - j ladder systems at low filling. *Physical Review B*, 108(15), oct 2023.
- [Bol21] Steffen Bollmann. Groundstate phase diagrams of variants of the two-leg t - j ladder at low fillings, October 2021.
- [BRvW19] Aron Beekman, Louk Rademaker, and Jasper van Wezel. An intro-

- duction to spontaneous symmetry breaking. *SciPost Physics Lecture Notes*, December 2019.
- [Com22] Roland Combescot. *Superconductivity: An Introduction*. Cambridge University Press, 2022.
- [CRI24] Sherry Choi and Lucy Readinig-Ikkanda. Itensor, high-performance tensor software inspired by tensor diagrams, may 2024.
- [CTDL07] Claude Cohen-Tannoudji, Bernard Diu, and Franck Laloë. *1 Welle und Teilchen*. Walter de Gruyter, dec 2007.
- [ECP10] J. Eisert, M. Cramer, and M. B. Plenio. Colloquium: Area laws for the entanglement entropy. *Reviews of Modern Physics*, 82(1):277–306, February 2010.
- [Ess] F.H.L. Essler. Statistical mechanics and phase transitions. <http://www-thphys.physics.ox.ac.uk/people/FabianEssler/C6web2012/StatMech.pdf>. Last accessed 2024-07-17.
- [Fli18] Torsten Fließbach. *Quantenmechanik: Lehrbuch zur Theoretischen Physik III*. Springer Berlin Heidelberg, 2018.
- [FWS22a] Matthew Fishman, Steven R. White, and E. Miles Stoudenmire. Codebase release 0.3 for ITensor. *SciPost Phys. Codebases*, pages 4–r0.3, 2022.
- [FWS22b] Matthew Fishman, Steven R. White, and E. Miles Stoudenmire. The ITensor Software Library for Tensor Network Calculations. *SciPost Phys. Codebases*, page 4, 2022.
- [GM14] Rudolf Gross and Achim Marx. *Festkörperphysik*. de Gruyter Studium. Walter de Gruyter, 2 edition, October 2014.
- [Gri05] David J. Griffiths. *Introduction to Quantum Mechanics*. Pearson Prentice Hall, 2nd edition, 2005.
- [GWX⁺24] Jun Ge, Pinyuan Wang, Ying Xing, Qiangwei Yin, Anqi Wang, Jie Shen, Hechang Lei, Ziqiang Wang, and Jian Wang. Charge-4e and charge-6e flux quantization and higher charge superconductivity in kagome superconductor ring devices. *Phys. Rev. X*, 14:021025, May 2024.

- [HHC⁺12] Tian-Heng Han, Joel S. Helton, Shaoyan Chu, Daniel G. Nocera, Jose A. Rodriguez-Rivera, Collin Broholm, and Young S. Lee. Fractionalized excitations in the spin-liquid state of a kagome-lattice anti-ferromagnet. *Nature*, 492(7429):406–410, December 2012.
- [Hoh67] P. C. Hohenberg. Existence of long-range order in one and two dimensions. *Phys. Rev.*, 158:383–386, Jun 1967.
- [Isi25] Ernst Ising. Beitrag zur theorie des ferromagnetismus. *Z. Phys.*, 31(1):253–258, feb 1925.
- [KKN⁺14] B. Keimer, S. A. Kivelson, M. R. Norman, S. Uchida, and J. Zaanen. High temperature superconductivity in the cuprates, 2014.
- [Köh19] Thomas Köhler. *Photoexcitations of model manganite systems using matrix-product states*. PhD thesis, 2019.
- [Lan50] C Lanczos. An iteration method for the solution of the eigenvalue problem of linear differential and integral operators. *J. Res. Natl. Bur. Stand. (1934)*, 45(4):255, oct 1950.
- [Man22] Salvatore R. Manmana. *Computational Physics I + II*. Philipps-Universität Marburg, 2022.
- [MMGH17] Salvatore R. Manmana, Marcel Möller, Riccardo Gezzi, and Kaden R. A. Hazzard. Correlations and enlarged superconducting phase of $t - J_{\perp}$ chains of ultracold molecules on optical lattices. *Phys. Rev. A*, 96:043618, Oct 2017.
- [MMM11] Alexander Moreno, Alejandro Muramatsu, and Salvatore R. Manmana. Ground-state phase diagram of the one-dimensional t - j model. *Phys. Rev. B*, 83:205113, May 2011.
- [Mou04] Andrei Mourachkine. *Room-temperature superconductivity*. Cambridge International Science Publishing, Cambridge, England, January 2004.
- [MSF⁺14] R. Mankowsky, A. Subedi, M. Först, S. O. Mariager, M. Chollet, H. T. Lemke, J. S. Robinson, J. M. Glownia, M. P. Minitti, A. Frano, M. Fechner, N. A. Spaldin, T. Loew, B. Keimer, A. Georges, and A. Cavalleri. Nonlinear lattice dynamics as a basis for enhanced superconductivity in $\text{YBa}_2\text{Cu}_3\text{O}_{6.5}$. *Nature*, 516(7529):71–73, Dec 2014.

- [MW66] N. D. Mermin and H. Wagner. Absence of ferromagnetism or antiferromagnetism in one- or two-dimensional isotropic heisenberg models. *Phys. Rev. Lett.*, 17:1133–1136, Nov 1966.
- [NDY⁺22] Titus Neupert, M. Michael Denner, Jia-Xin Yin, Ronny Thomale, and M. Zahid Hasan. Charge order and superconductivity in kagome materials. *Nature Physics*, 18(2):137–143, Feb 2022.
- [OLSA91] Masao Ogata, M. U. Luchini, S. Sorella, and F. F. Assaad. Phase diagram of the one-dimensional t-j model. *Phys. Rev. Lett.*, 66:2388–2391, May 1991.
- [Pae20] Sebastian Paeckel. *Topological and non-equilibrium superconductivity in low-dimensional strongly correlated quantum systems*. PhD thesis, 2020.
- [PKS⁺19] Sebastian Paeckel, Thomas Köhler, Andreas Swoboda, Salvatore R. Manmana, Ulrich Schollwöck, and Claudius Hubig. Time-evolution methods for matrix-product states. *Annals of Physics*, 411:167998, 2019.
- [PO56] Oliver Penrose and Lars Onsager. Bose-einstein condensation and liquid helium. *Phys. Rev.*, 104:576–584, Nov 1956.
- [Sac11] Subir Sachdev. *Quantum Phase Transitions*. Cambridge University Press, 2 edition, 2011.
- [Sch11] Ulrich Schollwöck. The density-matrix renormalization group in the age of matrix product states. *Annals of Physics*, 326(1):96–192, 2011. January 2011 Special Issue.
- [Sch24] Ulrich Schneider. Optical kagome lattice, Apr 2024.
- [Sto17] Miles Stoudenmire. Choosing dmrg parameters, January 2017.
- [SW78] R.F. Streater and A.S. Wightman. *PCT, spin and statistics and all that*. Benjamin/Cummings Publ., Boulder, CO, 1978.
- [TCY⁺22] Xiaokun Teng, Lebing Chen, Feng Ye, Elliott Rosenberg, Zhaoyu Liu, Jia-Xin Yin, Yu-Xiao Jiang, Ji Seop Oh, M. Zahid Hasan, Kelly J. Neubauer, Bin Gao, Yaofeng Xie, Makoto Hashimoto, Donghui Lu, Chris Jozwiak, Aaron Bostwick, Eli Rotenberg, Robert J. Birgeneau,

- Jiun-Haw Chu, Ming Yi, and Pengcheng Dai. Discovery of charge density wave in a kagome lattice antiferromagnet. *Nature*, 609(7927):490–495, Sep 2022.
- [Tim24] John Timmer. 25 years on, the search for higher-temp superconductors continues, may 2024.
- [WS98] Steven R. White and D. J. Scalapino. Density matrix renormalization group study of the striped phase in the 2d $t - J$ model. *Phys. Rev. Lett.*, 80:1272–1275, Feb 1998.
- [XCW⁺24] Yaofeng Xie, Nathan Chalus, Zhiwei Wang, Weiliang Yao, Jinjin Liu, Yugui Yao, Jonathan S. White, Lisa M. DeBeer-Schmitt, Jia-Xin Yin, Pengcheng Dai, and Morten Ring Eskildsen. Conventional superconductivity in the doped kagome superconductor $\text{cs}(\text{v}0.86\text{ta}0.14)\text{3sb}5$ from vortex lattice studies. *Nature Communications*, 15(1):6467, Jul 2024.
- [Yan62] C. N. Yang. Concept of off-diagonal long-range order and the quantum phases of liquid he and of superconductors. *Rev. Mod. Phys.*, 34:694–704, Oct 1962.
- [YYWW24] Qing-Geng Yang, Meng Yao, Da Wang, and Qiang-Hua Wang. Charge bond order and s -wave superconductivity in the kagome lattice with electron-phonon coupling and electron-electron interaction. *Phys. Rev. B*, 109:075130, Feb 2024.
- [ZR88] F. C. Zhang and T. M. Rice. Effective hamiltonian for the superconducting cu oxides. *Phys. Rev. B*, 37:3759–3761, Mar 1988.

Research Data Management

The data, plots and code can be found in the following git repository:

<https://gitlab.gwdg.de/justin.kowalski/ground-state-phases-of-the-t-j-model-on-kagome-strips>.

All important data will be stored in the 10-year archive provided by the IT service of the Institute of Theoretical Physics at the Georg-August-Universität Göttingen.

Acknowledgements

I appreciate all the people who supported me during this thesis period. First of all, I would like to thank my first referee and supervisor apl. Prof. Dr. Salvatore R. Manmana. His support, patience and the numerous discussions helped me a lot, not only in this research project, but also to form a profound view about physics and its working methods in general.

I am also grateful to Prof. Dr. Stefan Kehrein for being my second referee and for his exceptional lectures on quantum mechanics.

I would like to thank all group members for the insightful discussions, perspectives on interesting topics and the constant encouragements for solving challenges in my topic, especially to Manuel Buriks and Karun Gadge for also proofreading my chapter.

In the end, I want to thank my family and friends for their support during my three years studying physics and for their help in proofreading this thesis, especially to Maximilian Hecker and Jacob Winter, to complete my bachelor's degree.

Erklärung Ich versichere hiermit, dass ich die vorliegende Arbeit ohne fremde Hilfe selbstständig verfasst und nur die von mir angegebenen Quellen und Hilfsmittel verwendet habe. Wörtlich oder sinngemäß aus anderen Werken entnommene Stellen habe ich unter Angabe der Quellen kenntlich gemacht. Die Richtlinien zur Sicherung der guten wissenschaftlichen Praxis an der Universität Göttingen wurden von mir beachtet. Eine gegebenenfalls eingereichte digitale Version stimmt mit der schriftlichen Fassung überein. Mir ist bewusst, dass bei Verstoß gegen diese Grundsätze die Prüfung mit nicht bestanden bewertet wird.

Göttingen, den 3. August 2024

(Justin Kowalski)